Journal of Marine Research, 52, 909–946, 1994

Measurements of internal wave band eddy fluxes above a sloping bottom

by Hans van Haren[1,2], Neil Oakey[3] and Chris Garrett[1]

ABSTRACT

The boundary layer near a sloping bottom may have a major influence on the ocean's interior density structure (due to "boundary mixing") and on its circulation (because of the arrest of the Ekman layer by buoyancy forces). As a first attempt to measure eddy fluxes of momentum and buoyancy, in order to quantify the mixing in this region, we have carried out a 5-day pilot experiment on a sloping side of Emerald Basin on the Scotian Shelf. A moored upward-looking 1.2 MHz ADCP and a thermistor chain mounted along its vertical axis returned analyzable data between 8 and 17 m above the bottom at one-minute intervals. An extensive set of microstructure profiles was also obtained. The predominantly tidal flow regime causes the bottom boundary layer thickness to vary between $3 < z < 30$ m, with most high frequency activity during the upslope phase.

A bottom-normal momentum flux significantly different from zero is found in the cross-isobath direction only. The main contribution comes from a band near the buoyancy frequency N, possibly indicative of advective or Kelvin-Helmholtz instability. When cast in terms of mean-flow shear, the stress yields an eddy viscosity $A \approx 9 \times 10^{-3}$ m^2 s^{-1} within the boundary layer and twice this value at $z = 15$ m, the average height of the pycnocline that caps the boundary layer. The buoyancy flux also seems to be dominated by fluctuating signals near N, but is countergradient and only significantly different from zero at a height of about 15 m. The associated restratification occurs in short periods of approximately one hour when isotherms rise rapidly. Indirect evidence for the importance of the tertiary circulation within the boundary layer is found from the gradient of stress divergence and the mean bottom-normal velocity.

An approximate turbulent kinetic energy balance has been investigated, with the currents split into three parts (mean, tidal, and the high frequency part of the internal waveband ("turbulence")). Production balances viscous dissipation within a factor of 2. Turbulent kinetic energy production by interaction between the turbulent Reynolds stress and the mean flow shear and tidal shear are of the same order of magnitude, but the buoyancy term appears to be of equal importance at the pycnocline.

1. School of Earth and Ocean Sciences, University of Victoria, Victoria, B.C., V8W 2Y2, Canada.
2. Present address: Netherlands Institute for Sea Research, P.O. Box 59, 1790 AB Den Burg, The Netherlands.
3. Physical and Chemical Sciences, Department of Fisheries and Oceans, Bedford Institute of Oceanography, Dartmouth, N.S., B2Y 4A2, Canada.

1. Introduction

The focus of this paper is on estimates of bottom-normal velocity fluctuations and eddy momentum fluxes from the internal wave band above a sloping bottom. The sloping regions of ocean basins are of interest because much of the diapycnal transport of properties in the ocean may occur near its boundaries rather than in the interior. Recent theoretical studies (e.g. Phillips *et al.,* 1986; Garrett, 1990, 1991) have shown that the highly turbulent region produced by bottom friction very close to a boundary may not be effective in producing a flux of density as the water is already well mixed. There may be a region near a sloping boundary, however, within which mixing is still reasonably vigorous but buoyancy-driven flows, up and down the slope, continually restore at least part of the stratification. In such circumstances the mixing can produce a significant buoyancy flux in a way which will not occur above a flat bottom.

The mixing mechanism that is effective at some distance above the well-mixed region immediately adjacent to the bottom is expected to be associated with frequencies in the internal wave band, and arises from either vertical isopycnals (advective instability) or from billow formation (by Kelvin-Helmholtz shear instability) (Munk, 1981; Thorpe, 1978). The energy source is likely to be at lower frequencies, such as tidal or those at which internal waves are amplified on reflection from a slope (Thorpe, 1987; Eriksen, 1982, 1985).

Theoretical steady-state solutions (e.g. Garrett, 1991) show that the extent to which the water column restratifies, and hence the effectiveness of mixing near the boundary, depend on the profile of the eddy viscosity in the models, i.e. on (the divergence of) the eddy momentum flux. The eddy momentum and buoyancy fluxes near the bottom also affect the time it takes for a bottom Ekman layer to be arrested by buoyancy forces and hence cause the ocean bottom to be much more "slippery" for mean and low-frequency bottom currents than is normally assumed (MacCready and Rhines, 1993). Processes occurring near the sloping sea floor are thus central for questions of ocean circulation as well as mixing.

Establishing the eddy fluxes of buoyancy and momentum normal to the bottom to quantify the mixing requires the measurement, at high frequencies, of the water density and all three components of velocity, with measurement of the bottom-normal component presenting the greatest difficulty. To determine momentum fluxes, Gross *et al.* (1986) used acoustic travel time measurements to obtain all three components of the velocity, but were limited to within 5 m of the sea floor by the size of the tripod holding their instruments and so were essentially restricted to the mixed layer in which boundary-generated turbulence dominates. This regime was also studied by Lohrmann *et al.* (1990) using a 300 kHz pulse-to-pulse coherent Doppler sonar to achieve a vertical resolution of 0.2 m and a sampling rate adequate to resolve the dominant time scale of less than a minute but they, too, were limited to a range of

10 m which was within the well-mixed layer in their case. In both studies near-bottom momentum fluxes significantly different from zero were found.

In our pilot experiment we used a thermistor chain mounted along the vertical axis of a moored 1.2 MHz pulse-to-pulse incoherent four-beam acoustic Doppler current profiler (ADCP) with a potential range of 25 m and a sampling interval Δt of one minute. This excludes resolution of the full turbulence spectrum, but is adequate to resolve the internal wave band ($f < \sigma < N \ll 2\pi/\Delta t$, where σ is frequency and f denotes the Coriolis frequency).

A major consideration in attempts to measure eddy fluxes in the ocean is whether there is a "spectral gap" between the slowly-varying "mean" and the more rapidly varying fluctuations. Such a gap need not exist in the energy spectrum, but is required in any spatially divergent component of the eddy momentum flux (Reynolds stress), or eddy buoyancy flux, that might affect the mean. In the absence of a spectral gap statistically reliable estimates of the eddy fluxes cannot be obtained with an averaging time shorter than that over which the "mean" changes significantly.

In practice a spectral gap typically exists between inertio-internal motion (with frequencies greater than f) and low frequency mesoscale motions. In many situations, however, the inertio-internal band is dominated by a single frequency, perhaps inertial or, more commonly, tidal, and one may be interested in the effect of higher frequencies on this. In the absence of a spectral gap in this case (as for the turbulent boundary layer caused by a tidal current in homogeneous water (Heathershaw and Simpson, 1978)) one could resort to ensemble averaging of the Reynolds stress measured for short blocks of time at the same phase of successive tidal cycles, but this requires records longer than we have from this experiment.

Alternatively, one might omit intermediate (e.g. tidal) frequencies to see if the eddy fluxes that *can* be resolved before the "mean" flow changes also show a correlation with the mean current or shear. We shall examine this possibility further in this paper, defining the mean as the average over, say, three days rather than tidal periods. The main emphasis, however, will be on the statistical significance of Reynolds stress estimates, rather than a precise establishment of their generating sources.

The details of the observational program are described in Section 2 followed by theoretical and practical accounts of obtaining eddy momentum fluxes from ADCP data in Sections 3 and 4, respectively. In Section 5 we discuss some properties of the physical environment and relate these to some characteristics of a bottom boundary layer above a slope. In Section 6 the results on eddy momentum and buoyancy fluxes are discussed. Also in that section we summarize turbulent energy dissipation data that were obtained during the experiment, recognizing that the dissipation is not necessarily a manifestation of interaction between the Reynolds stress and the rate of strain of the mean flow, but could arise from breaking internal waves even in the

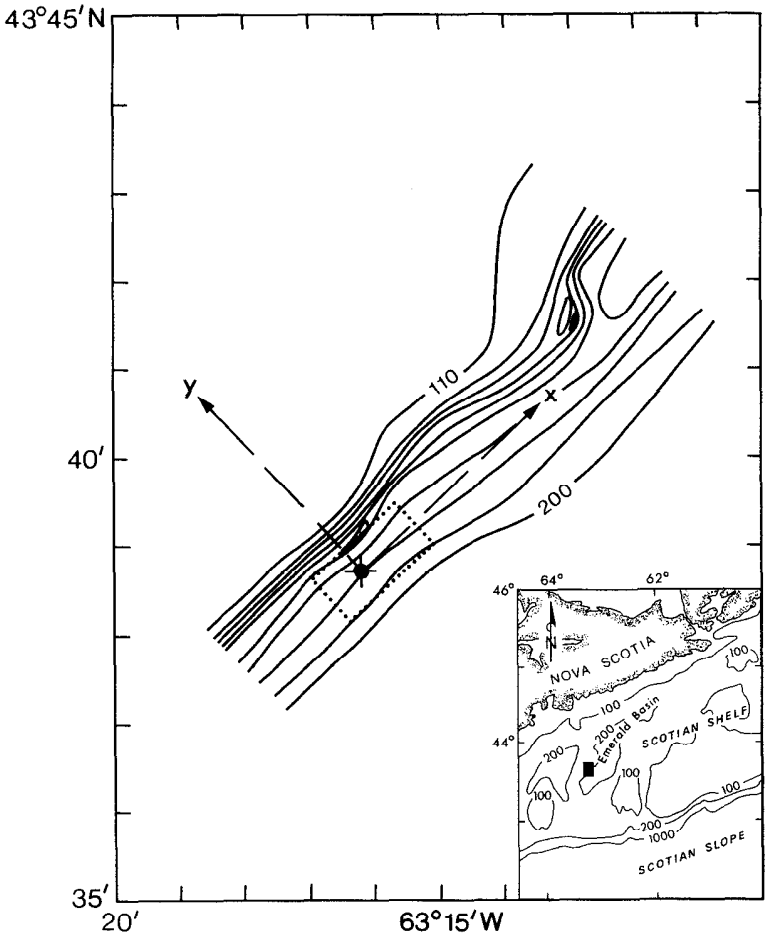

Figure 1. Detailed bottom topography and mooring site (⊕) in the experimental area on the Scotian Shelf (rectangle in insert) (isobaths in meters). Microstructure and CTD data were obtained outside the area of the dotted rectangle.

absence of a mean shear. The paper concludes with what we have learned from a pilot experiment and recommendations for a more definitive observational program.

2. Experimental set-up

An ADCP, thermistor chain and current meter were moored from October 10–15, 1990, on a sloping side of Emerald Basin on the Scotian Shelf (Fig. 1). Data were collected from the C. S. S. *Dawson* with a Guildline CTD and EPSONDE, a free-falling microstructure profiler (Oakey, 1987). Prior to deployment of the mooring a bathymetric map (Fig. 1) was constructed from echosounder data along transects approximately across the isobaths and 1 km apart. The isobaths show little

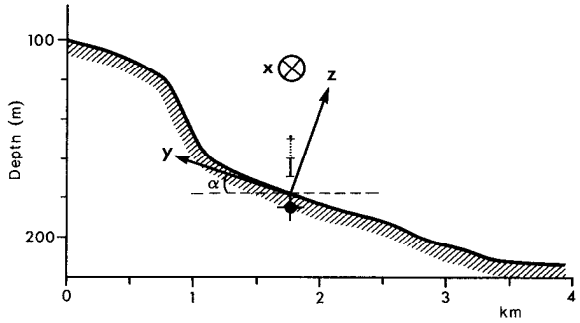

Figure 2. Cross-slope bottom profile measured along a transect through the mooring site (◆). The local bottom slope angle is α. The vertical bar indicates the part of the water column from which useful ADCP data were collected; the dot indicates the depth of the current meter and the dotted line, the extent of the thermistor chain.

variability in the along-slope direction. At the mooring site the slope measured $\sin\alpha = 0.024 \pm 0.004$ ($\alpha = 1.4° \pm 0.2°$), with α the angle to the horizontal (Fig. 2). For this slope the Burger number $S = N^2 \sin^2\alpha / f^2 \simeq 1.4$ ($f = 1.007 \times 10^{-4}$ s^{-1}; $N = 5 \pm 1 \times 10^{-3}$ s^{-1} from CTD measurements) and is not small. Thus the characteristics of the boundary layer, such as the mixed layer height, should differ from those on a flat bottom (Garrett, 1990).

The group velocity of internal gravity waves of frequency σ, propagating in a uniformly stratified inviscid fluid, is inclined to the horizontal at an angle α_I, for which

$$\sin^2\alpha_I = \frac{(\sigma^2 - f^2)}{(N^2 - f^2)}. \tag{1}$$

Linear theory predicts that the wavenumber, shear and energy density of such waves reflected from a uniform slope at an angle α increase considerably when $\alpha_I \rightarrow \alpha$ (Eriksen, 1985). Near our mooring we find that for semidiurnal internal tides $\sin\alpha_I = 0.020 \pm 0.004$. Thus, within the accuracy of determination of the bottom slope and stratification rate, the site is near-critical for internal waves at tidal frequencies and may thus provide an environment favorable for higher frequency internal wave instability. It should be noted that although the slope is locally uniform, a major topographic change is only 600 m away in the cross-isobath direction (Fig. 2). Between 110–150 m depth the slope is $\sin\alpha \approx 0.12$ and is near-critical for frequencies $\sigma = 6.1 \pm 1.2 \times 10^{-4}$ s^{-1}. The concave shape of the topography may be less favorable for the shear enhancement and associated mixing upon wave reflection (Gilbert and Garrett, 1989).

The subsurface mooring consisted of a 1.2 MHz RD Instruments upward-looking ADCP with an Aanderaa thermistor chain mounted above it, along its central axis (Fig. 3). Thermistors were separated by 3 m, except near the ADCP where their

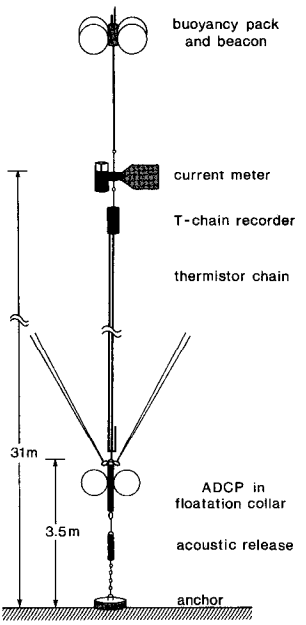

Figure 3. Mooring diagram (instruments not to scale). Thermistors are located every 3 m in their chain. Doubling the thermistor chain provided a higher vertical resolution of temperature sampling over a distance of 5 m above the ADCP.

intervals were reduced by doubling the chain. The ADCP was fitted with a floatation collar; the tilt was never more than 4°. Unfortunately, the lack of a tail fin allowed the instrument to spin freely at a typical rate of several degrees per minute. Just below the buoyancy package at the top of the mooring was an Aanderaa RCM-8 current meter. Within this mooring configuration the water column was sampled between 5 and 31 m above the bottom.

In Table 1 some characteristics of the site and the ADCP are given. Ensembles of velocity data were stored every minute for 1-m depth intervals and consisted of three components $\hat{u}, \hat{v}, \hat{w}$, in a coordinate system fixed relative to the earth, and an "error" velocity $\hat{e}$. The latter is proportional to the difference between the vertical velocity components estimated along the two planes of the instrument. We use a hat notation to denote instrumental output; velocity components without a hat denote the unknown 'true' velocity field, which is defined as the water velocity occurring within a depth cell and unbiased by instrumental noise. Instrumental noise, typically large for a pulse-to-pulse incoherent sonar, and finite storage capacity prevented a "sampling" faster than once per minute. This excluded resolution of all the turbulent motion but gave a Nyquist frequency of about $10\,N$. At this sampling rate the nominal error amounts to ± 1.1 cm s^{-1} in $\hat{u}, \hat{v}$ and to ± 0.4 cm s^{-1} in $\hat{w}, \hat{e}$ for a data harvest of 90% per ensemble.

The data have been transformed to the Cartesian righthanded coordinate system

Table 1. Site and ADCP specifications.

position	43°38.72'N 63°16.26'W
water depth; bottom slope	178 m; $\sin\alpha = 0.024 \pm 0.004$
ADCP type	RDI-ADCP//SN-239//1228.8 kHz
beam inclination	30°
ping frequency	3 Hz
ensemble (sample)	180 pings maximum (1 min)
record length	10/10/90 13:12GMT to 15/10/90 11:50GMT (7090 samples)
pulse/depth cell length	1 m (15% overlap)
first depth cell	1.5 m above head (z = 5 m)
nominal range	25 depth bins
useful data range	depth bins 4–17 (z = 8–21 m)*
tilt sensor accuracy	1°
low-pass tracking filter (LPF)	enabled throughout acquisition range
"time" constant LPF	3.5 m
filter mode	narrowband

*See Section 4 for details.

in Figures 1, 2 so that u, v are along and across the isobaths respectively and w is perpendicular to the slope. This choice is appropriate if at least the statistics of the flow are assumed independent of the x, y-coordinates in the plane of the slope.

3. ADCP probing definitions

In experiments on Reynolds stress estimates from four-beam ADCP data it is unnecessary to assume that each beam measures the same instantaneous velocity field; this would restrict the resolved horizontal scales to twice the beam spread of about 10 to 100 m. It is necessary, however, to assume statistical homogeneity in a plane parallel to the surface or bottom (Lohrmann *et al.*, 1990; Plueddemann, 1987).

After the emission of a sound pulse (ping) an ADCP registers the backscattered signal for each depth bin and computes a speed from the Doppler-shifted frequency. For each of the four beams, i = 1 to 4, velocity components $\hat{b}_{ij}$ are obtained, where j denotes the depth bin. These water velocity measurements assume passive scatterers, typically plankton.

Each $\hat{b}_i$ (for any bin, so we drop the index j) is composed of two velocity components in the Cartesian coordinate system of the instrument (Fig. 4) and an instrumental error $\hat{\gamma}_i$. We start with the assumption that the ADCP is fixed relative to the earth and oriented along the coordinates in Figure 2, i.e. with its vertical axis aligned along z. Then,

$$\begin{aligned} \hat{b}_1 &= -u_1 \sin\theta - w_1 \cos\theta + \hat{\gamma}_1 \\ \hat{b}_2 &= u_2 \sin\theta - w_2 \cos\theta + \hat{\gamma}_2 \\ \hat{b}_3 &= -v_3 \sin\theta - w_3 \cos\theta + \hat{\gamma}_3 \\ \hat{b}_4 &= v_4 \sin\theta - w_4 \cos\theta + \hat{\gamma}_4 \end{aligned} \tag{2}$$

in which θ is the orientation of the beams with respect to the vertical axis. Average

velocity components over the beam spread are obtained, after dropping the $\hat{\gamma}_i$ for clarity (which may not be small, but rather, which are unknown), according to

$$\begin{aligned}
\frac{(\hat{b}_2 - \hat{b}_1)}{2\sin\theta} &= \frac{(u_1 + u_2)}{2} - \frac{(w_2 - w_1)}{2\tan\theta} = u + \delta_u \equiv \hat{u} \\
\frac{(\hat{b}_4 - \hat{b}_3)}{2\sin\theta} &= \frac{(v_4 + v_3)}{2} - \frac{(w_4 - w_3)}{2\tan\theta} = v + \delta_v \equiv \hat{v} \\
\frac{-\sum_{i=1}^{4} \hat{b}_i}{4\cos\theta} &= \frac{\sum_{i=1}^{4} w_i}{4} - \frac{[(v_4 - v_3) + (u_2 - u_1)]\tan\theta}{4} = w + \delta_w \equiv \hat{w} \\
\frac{[\hat{b}_1 + \hat{b}_2 - (\hat{b}_3 + \hat{b}_4)]}{4\cos\theta} &= \frac{[w_3 + w_4 - (w_1 + w_2)]}{4} - \frac{[(v_4 - v_3) - (u_2 - u_1)]\tan\theta}{4} \equiv \hat{e}.
\end{aligned} \tag{3}$$

Here $\hat{u}$, $\hat{v}$, $\hat{w}$ are equal to correct values of the velocity components, provided that they are the same over the beam spread and that the instrumental errors are equal for the four beams. The deviations δ_k, $k = u, v, w$ include both "error" sources. The values u, v, w are indicated without a hat symbol because they represent velocities along the central vertical axis between the beams assuming that the horizontal gradients are close to linear. The "error" velocity $\hat{e}$ is generally considered redundant, but is important for estimating Reynolds stresses, as we shall see below. In fact, when one beam gives bad data, $\hat{u}$, $\hat{v}$, $\hat{w}$ are still obtained ("three beam solution"), resulting in a greater data harvest for these three components but not for $\hat{e}$. With the information from tilt sensors and flux gate compass, the $\hat{u}$, $\hat{v}$, $\hat{w}$ data from a tilted and rotating instrument are transferred to a coordinate system fixed relative to the earth before a new ping starts.

Lohrmann *et al.* (1990) provide equations for Reynolds stress estimates for an instrument that is fixed in space, here in the coordinates of Figure 2. Using the Reynolds decomposition of $\hat{b}_i = \overline{\hat{b}_i} + \hat{b}_i'$, and similarly for all velocity components, with the overbar denoting averaging over a certain length of time, we obtain (2) for the fluctuating beam velocities $\hat{b}_i'$. Suitable subtraction of their variances gives, after subtraction of the mean quantities, equations like

$$\begin{aligned}
\frac{(\overline{\hat{b}_2'^2} - \overline{\hat{b}_1'^2})}{2\sin 2\theta} &= -\frac{(\overline{u_1'w_1'} + \overline{u_2'w_2'})}{2} + \frac{(\overline{u_2'^2} - \overline{u_1'^2})\tan\theta}{4} \\
&\quad + \frac{(\overline{w_2'^2} - \overline{w_1'^2})}{4\tan\theta} \equiv -(\overline{u'w'})_b \\
\frac{(\overline{\hat{b}_4'^2} - \overline{\hat{b}_3'^2})}{2\sin 2\theta} &= -\frac{(\overline{v_3'w_3'} + \overline{v_4'w_4'})}{2} + \frac{(\overline{v_4'^2} - \overline{v_3'^2})\tan\theta}{4} \\
&\quad + \frac{(\overline{w_4'^2} - \overline{w_3'^2})}{4\tan\theta} \equiv -(\overline{v'w'})_b
\end{aligned} \tag{4}$$

where terms involving $\hat{\gamma}_i$ have been left out. The final, b-subindexed quantities consist

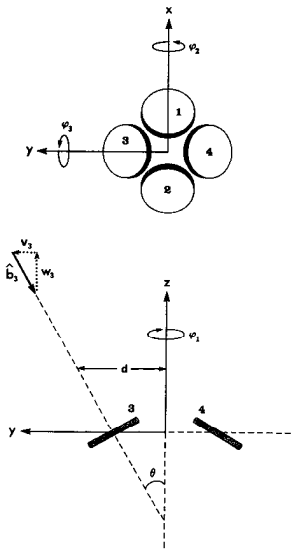

Figure 4. Decomposition of velocity components and definition sketch of beam orientation (θ) and rotation angles (heading φ_1, pitch φ_2, roll φ_3) in the local coordinate system of the ADCP.

of an average of vertical shear stress components estimated within the ensonified volume of each beam, provided the statistics of the fluctuating flow are homogeneous over the beam spread. In general $\overline{(u'w')}_b \neq \overline{(\hat{u}'\hat{w}')}$, the 'direct' stress estimates obtained by computing the covariance between $\hat{u}'$ and $\hat{w}'$. This also holds for the v-component.

Our instrument does not directly provide $\hat{b}_i$ but it stores $\hat{u}$, $\hat{v}$, $\hat{w}$, $\hat{e}$ data ensemble-averaged over one-minute intervals. Despite these limitations an estimate similar to (4) can be given. The essentials of the discussion do not alter if we assume here that our instrument is fixed in the coordinates of Figure 2 and has stored data at the ping rate. Rewriting (2) using (3) in terms of ensemble-averaged values gives

$$\begin{aligned} \hat{b}_1 &= -\hat{u}\sin\theta - (\hat{w} - \hat{e})\cos\theta \\ \hat{b}_2 &= \hat{u}\sin\theta - (\hat{w} - \hat{e})\cos\theta \\ \hat{b}_3 &= -\hat{v}\sin\theta - (\hat{w} + \hat{e})\cos\theta \\ \hat{b}_4 &= \hat{v}\sin\theta - (\hat{w} + \hat{e})\cos\theta. \end{aligned} \tag{5}$$

The shear stress estimates are readily obtained (cf. (4)) from

$$\begin{aligned} -\overline{(u'w')}_b &= \frac{(\overline{\hat{b}_2'^2} - \overline{\hat{b}_1'^2})}{2\sin 2\theta} = -\overline{\hat{u}'(\hat{w}' - \hat{e}')} \\ -\overline{(v'w')}_b &= \frac{(\overline{\hat{b}_4'^2} - \overline{\hat{b}_3'^2})}{2\sin 2\theta} = -\overline{\hat{v}'(\hat{w}' + \hat{e}')}. \end{aligned} \tag{6}$$

Thus, the error velocity is essential and relaxes the homogeneity condition.

Free spinning of the ADCP about its vertical axis requires a correction for the stress estimates. For a relatively slowly spinning instrument (at a rate of a few degrees per ensemble period), the approximately correct equivalent of (6) reads

$$\begin{aligned} -(\overline{u'w'})_b &= -\overline{\hat{u}'[\hat{w}' - \hat{e}'(\cos 2\varphi_1 - \hat{v}'/\hat{u}' \sin 2\varphi_1)]} \\ -(\overline{v'w'})_b &= -\overline{\hat{v}'[\hat{w}' + \hat{e}'(\cos 2\varphi_1 + \hat{u}'/\hat{v}' \sin 2\varphi_1)]}, \end{aligned} \tag{7}$$

where φ_1 is the heading angle measured by the instrument and stored per ensemble. This equation will be used henceforth. Its derivation is given in the Appendix. For our data the correction in (7) involving $\hat{e}'$ accounts for about 20% of the estimated stress.

The stress estimates defined above are prone to errors due to unfavorable flow conditions and instrumental flaws. For a tilted system, mistakenly treated as fixed in the coordinates of Figure 2, (6) becomes, to first order in φ_2, φ_3 (pitch (in the same plane as α) and roll angle, respectively; both small),

$$\begin{aligned} \frac{(\overline{\hat{b}_2'^2} - \overline{\hat{b}_1'^2})}{2 \sin 2\theta} &\simeq -(\overline{u'w'})_b - \varphi_3(\overline{u'\hat{u}'} - \overline{w'(\hat{w}' - \hat{e}')}) + \varphi_2\overline{\hat{u}'v'} \\ \frac{(\overline{\hat{b}_4'^2} - \overline{\hat{b}_3'^2})}{2 \sin 2\theta} &\simeq -(\overline{v'w'})_b + \varphi_2(\overline{v'\hat{v}'} - \overline{w'(\hat{w}' + \hat{e}')}) - \varphi_3\overline{u'\hat{v}'}, \end{aligned} \tag{8}$$

as given for (4) by Lohrmann *et al.* (1990). They point out that when (surface) waves are contained in the fluctuating (turbulence) part of the signal, the contributions of $\varphi_3 u'\hat{u}'$ and $\varphi_2 v'\hat{v}'$ may not be small, even for φ_2, φ_3 a few degrees. Thus, relatively accurate tilt sensors are required as well as a proper definition of a (tilted) coordinate system.

Fluctuating parts of the vertical velocity are also used to calculate buoyancy flux estimates by multiplying them at appropriate depth levels by $-\rho' = -0.127\ T'$ (cf. Section 5), where T' is obtained from thermistor chain data. The temperature data, originally sampled at $\Delta t = 2$ min intervals, have been upgraded prior to flux calculations. Firstly, the slow sensor response has been "corrected" according to

$$T_i = T_{(m)i} + \frac{\tau}{2\Delta t}(T_{(m)i+1} - T_{(m)i-1}), \tag{9}$$

where $T_{(m)i}$ denotes the ith sample of measured (m) temperature and $\tau = 1$ min (manufacturer) is the response time scale of the (embedded) thermistors. Secondly, the resulting T_i have been subsampled at one-minute intervals by linear interpolation.

As for Reynolds stress estimates, buoyancy flux estimates from ADCP and thermistor chain data require some assumptions because different volumes of water are sampled. The measured $\hat{w}$ represents true w along the central axis of the

mooring, where T (and thus ρ) is measured, plus errors due to the instrumental noise and the beam spread of the ADCP. The influence of current non-uniformity due to the latter can be estimated from the data, under certain conditions, so that the flux estimate can be corrected accordingly. We consider the estimate

$$\overline{\hat{w}'\rho'} = \overline{\left[\frac{\sum_{i=1}^{4} w_i'}{4} - \frac{\tan\theta}{4}(v_4' - v_3' + u_2' - u_1')\right]\rho'} \tag{10}$$
$$= \overline{w'\rho'} - \frac{\tan\theta}{4}\overline{(v_4' - v_3' + u_2' - u_1')\rho'}$$

in which (3) has been invoked. Again, terms containing the unknown $\hat{\gamma}_i$ are left out. Rewriting part of the second term on the right-hand side gives

$$\overline{(v_4' - v_3')\rho'} = \overline{v'(y - \delta y)\rho'(y) - v'(y + \delta y)\rho'(y)}$$
$$\approx -2\delta y \overline{\left[\rho' \frac{\partial v'}{\partial y}\right]},$$

where $\delta y = d$ denotes half the spread of the beams (Fig. 4). Then the true flux becomes

$$\overline{w'\rho'} \approx \overline{\hat{w}'\rho'} + \frac{\tan\theta}{2} d \overline{\left[\rho' \frac{\partial w'}{\partial z}\right]}, \tag{11}$$

using $\nabla \cdot \mathbf{u}' = 0$. For beams slanted at $\theta = 30°$, $d = (z - 3.5)/2$, with z the height above the bottom. Thus, the magnitude of the second term on the right-hand side of (11) depends on the vertical scale over which w' varies, which is not measured. A first guess would be z, so that this term becomes $O(10^{-1})$ times the other terms. To estimate the correction we replace w' with $\hat{w}' - \delta_{w'}$ in the last term of (11) and repeat the steps leading to (11) to obtain

$$\overline{w'\rho'} \simeq \overline{\hat{w}'\rho'} + \frac{\tan\theta}{2} d \overline{\left[\rho' \frac{\partial \hat{w}'}{\partial z}\right]} + \left(\frac{\tan\theta}{2} d\right)^2 \overline{\left[\rho' \frac{\partial^2 w'}{\partial z^2}\right]} \tag{12}$$

where the last term may be dropped when the ratio of the first two terms on the right-hand side is small. This ratio has been calculated using finite differences over 2 m intervals and the correction term measures roughly $0.1\,\overline{\hat{w}'\rho'}$, as anticipated.

4. Data handling

a. Useful ADCP data. Only ADCP data from bins 4 to 13 (z = 8 to 17 m) were of sufficient quality to estimate Reynolds stresses. Data above bin 17 were too noisy to process. From bins 14 to 17 the number of velocity estimates obtained from the three

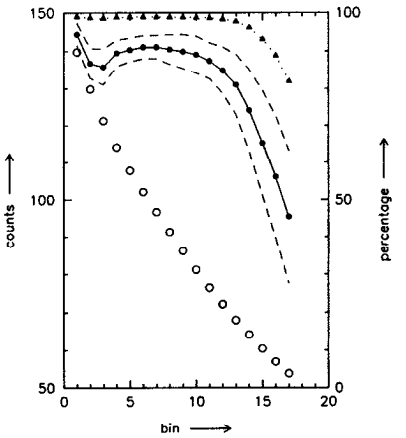

Figure 5. Mean values of some data quality indicators for the first 17 bins. "AGC," a measure of the backscatter strength, is shown by ○ (1 count ≈ 0.47 dB). The percentage of good data per ensemble is shown for current components estimated from four beams (●; with the standard deviation indicated by the dashed lines) and from either three or four beams (▲).

beam solution greatly exceeded those from four beams (Fig. 5). Presumably the water column was depleted in scatterers leading to the low value of backscatter as indicated by the ADCP's automatic gain control ('AGC', Fig. 5) and on the ship's echosounder. Previous and later uses of the same ADCP yielded much higher backscatter. The intended comparison between data from an upper bin of the ADCP and from the current meter thus could not be performed because of the 10 m data gap.

The lowest three bins were rejected because of unrealistic velocity signals best exemplified by the low-frequency $\hat{w}$ and $\hat{e}$ (Fig. 6). These point to unevenly spread instrumental noise. It is a common observation that the first bin returns bad data (e.g. Schott, 1988; Lohrmann *et al.,* 1990), but a comprehensive explanation has not yet been given. Flagg and Smith (1989) credit "residual transducer ringing" as a cause but do not elaborate. Chereskin *et al.* (1989) and RDI (1989) indicate that skewing of the Doppler signal may occur due to misadjustment of the low-pass tracking filter when measurements are made in shear flows. It affects especially the lowest bin and will generally result in less apparent shear. It may not show up in $\hat{w}$, $\hat{e}$ when all four beams are equally affected. In our case, only beam 3 returned bad data in the lowest bin, as was revealed by recomputing the radial beam velocities $\hat{b}_i$ from $\hat{u}$, $\hat{v}$, $\hat{w}$, $\hat{e}$ relative to the orientation of the instrument and using tilt and heading information.

Although we do not fully understand the nature of this noise, the erroneous signal seems a result of advection of different amounts of scatterers, related to flow and water mass, since records of temperature, percentage of good data, and backscatter strength all resemble the time variability of $\hat{w}$ and $\hat{e}$ in bin 1. More interestingly, the

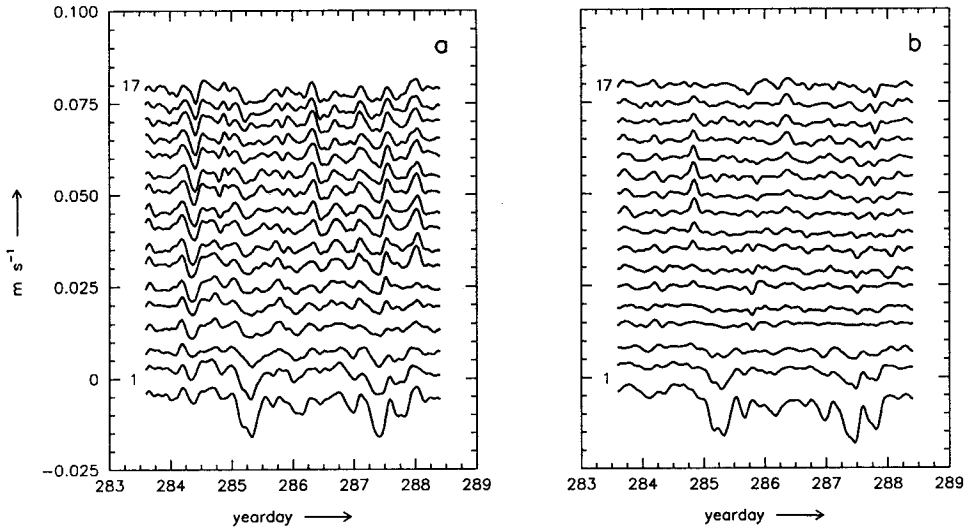

Figure 6. Two-hourly smoothed time series of $\hat{w}$ (a) and error $\hat{e}$ (b) velocity for bins 1–17 ($5 \leq z \leq 21$ m). The vertical scale is proper for bin 1. The relative offset of the other bins is 0.005 m s^{-1}.

error disappears above bin 4 (one "tracker time constant" above bin 1) and $\hat{w}$ and $\hat{e}$ differ above this height (Fig. 6).

Above $z = 9$ m low frequency non-white noise contaminated estimates of mean $\overline{\hat{w}}$ and $\overline{\hat{e}}$ in an equal sense, but with opposite sign. The associated error prevents estimates of $\overline{\hat{w}}$ to better than $\pm 3 \times 10^{-4}$ m s^{-1}, which is about an order of magnitude larger than the nominal error ($\simeq 5 \times 10^{-5}$ m s^{-1}). The sign difference between $\overline{\hat{w}}$ and $\overline{\hat{e}}$ points to a larger contamination in beams 1 and 2 than in the other two, on average, and a proper correction seems to be $\overline{\hat{w}}_c = \overline{\hat{w}} + \overline{\hat{e}}$, with a reduced error as estimated from its vertical profile of about $\pm 8 \times 10^{-5}$ m s^{-1}.

Indications of errors in tilt sensors or beam orientation, which may cause horizontal currents to appear in the $\hat{w}$-data, were not found. Another possible non-physical vertical velocity signal may be caused by free planktonic migration, which would primarily occur at diurnal periods (Schott and Johns, 1987; Flagg and Smith, 1989). However, no such regular pattern could be detected from the vertical velocity data.

Finally, apparent current inhomogeneity over the beam spread may be introduced in the ADCP data by instrumental noise unevenly spread over the beams. Reflection from a tilted thermistor chain could cause this, but Schott (1988) has found the effect to be negligible. We could not find any effects of the thermistor chain in our data.

b. Practical Reynolds decomposition. Decomposition of the current components into a statistically steady (mean) and a fluctuating part depends on the physical definitions of both flow components and their interaction, and on a proper separation

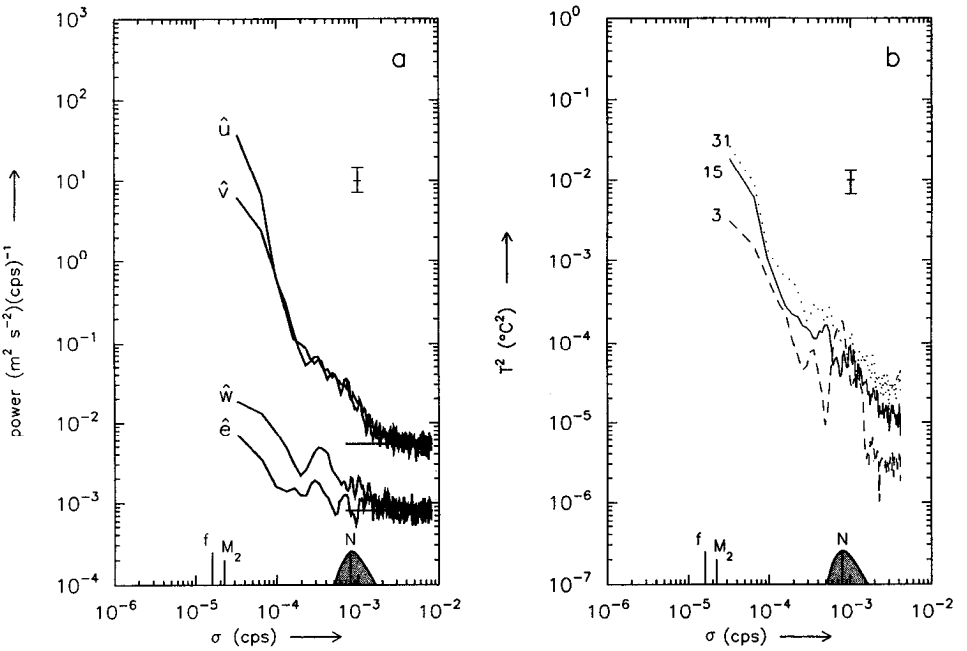

Figure 7. (a) Autospectra computed from full length records of $\hat{u}, \hat{v}, \hat{w}, \hat{e}$ at bin 11 (z = 15 m). (b) Variance preserving spectra from full length temperature records measured at z = 3 m (ADCP), z = 15 m (T-chain), z = 31 m (RCM). Smoothing is performed by averaging spectral estimates of ½-day data pieces, weighted by a full cosine bell and overlapping each other by half their length; 95% confidence intervals are shown by vertical bars. A most likely distribution of the buoyancy frequency N is given at the x-axis.

between the two appearing as a well defined spectral gap. Figure 7 shows that physical signals are indistinguishable from instrumentally-caused white noise at frequencies just greater than $N = N(z,t)$. (For general purposes an average N of 5×10^{-3} s^{-1} is used, but, when appropriate, we use $N(z)$.) Standard deviations calculated from the flat high frequency tail of the autospectra for ADCP data compare well with the nominal errors given in Section 2. A well defined gap is not apparent in the autospectra. Within the internal wave band the spectra for the horizontal current components fall off as σ^{-n}, $n \simeq 2$ to 2.5, at frequencies higher than M_2. The only, weakly, distinct feature is a sudden transition to $n \simeq 1$ at 1.5×10^{-4} cps. The band between this frequency and N has a uniform shape and power content for the horizontal current components as a function of depth, but shows significant elevations in the vertical velocity spectrum only for bins 9 to 13 ($13 < z < 17$ m), with the most pronounced shown in Figure 7. The small significant peak at 3×10^{-4} cps (2×10^{-3} s^{-1}) may represent a Doppler-shifted (instability) frequency. It may also represent high frequency internal lee waves generated by the large-scale flow over small-scale topography (Thorpe, 1992). In that case, given the mean flow amplitude, the effective topographic length scale is 100 m which we did not resolve

with our echo soundings. Given the $\hat{w}$-amplitude at 3×10^{-4} cps, the topographic amplitude should be about 1.5 m, resulting in a possible lee wave stress of 3×10^{-6} m^2 s^{-2} (Thorpe, 1992; Section 6).

Temperature spectra show a significant increase near N, but close to the bottom only. Higher up in the water column more of the internal wave band is filled, probably due to Doppler smearing and with an apparent shift from N to $\frac{1}{2}N$ and again showing a kink near 10^{-4} cps.

Although the coherence at each frequency is less than significant, a broad band near N exists where the cospectrum for $(vw)_b$ tends to be negative (Fig. 8). We thus sacrifice frequency resolution and examine the (zero-lag) covariances between fluctuating quantities for significance.

The flow is separated at the kink in the (internal wave) spectrum (Fig. 9). The cutoff frequency is 1.2×10^{-4} cps. Thus the band near N is considered part of the high-pass or fluctuating signal. High frequency noise is not filtered out, because little contribution to covariance estimates is expected from this part of the spectrum. We used a linear-phase symmetric filter to avoid introduction of contaminating phase changes. The filter was sharpened by varying its length and a Kaiser window reduced leakage (Parks and Burrus, 1987). Data loss amounted to ¾ days at both ends of the time series.

c. Test for statistical significance. The Reynolds stresses are estimated from the covariances between fluctuating velocity components according to (7) and from the covariances between $\hat{v}'$ (and $\hat{u}'$) and $\hat{w}'$ with the assumption of spatial uniformity of the current itself.

As the spectra of the fluctuating velocity components are red, the variance of the covariance estimates could not be computed from the product of the two autocovariances (Jenkins and Watts, 1968). In order to test for zero true covariance, we compared the zero lag covariance estimates with the distribution of estimates computed at non-zero lag (Fig. 10; Barry Ruddick, pers. comm.). A pseudo-random generator was used to determine a distance over which to shift the time series with respect to each other. A zone of on average 10 points near zero lag was excluded in which the autocorrelation function was above a criterion level of 0.05. This computation was repeated 1000 times for each stress estimate, which was sufficient to provide a quasi-normal 'error distribution'.

We return to the numerical estimates of stress and buoyancy flux in Section 6 after first describing the mean oceanographic conditions.

d. Microstructure data. EPSONDE (Oakey, 1987) was deployed to measure velocity and temperature microstructure to within 15 cm of the bottom while the ship drifted, mostly in the cross-isobath direction. On average, measurements were made at a distance of 3 km from the mooring, to avoid entangling of instruments (Fig. 1). Some

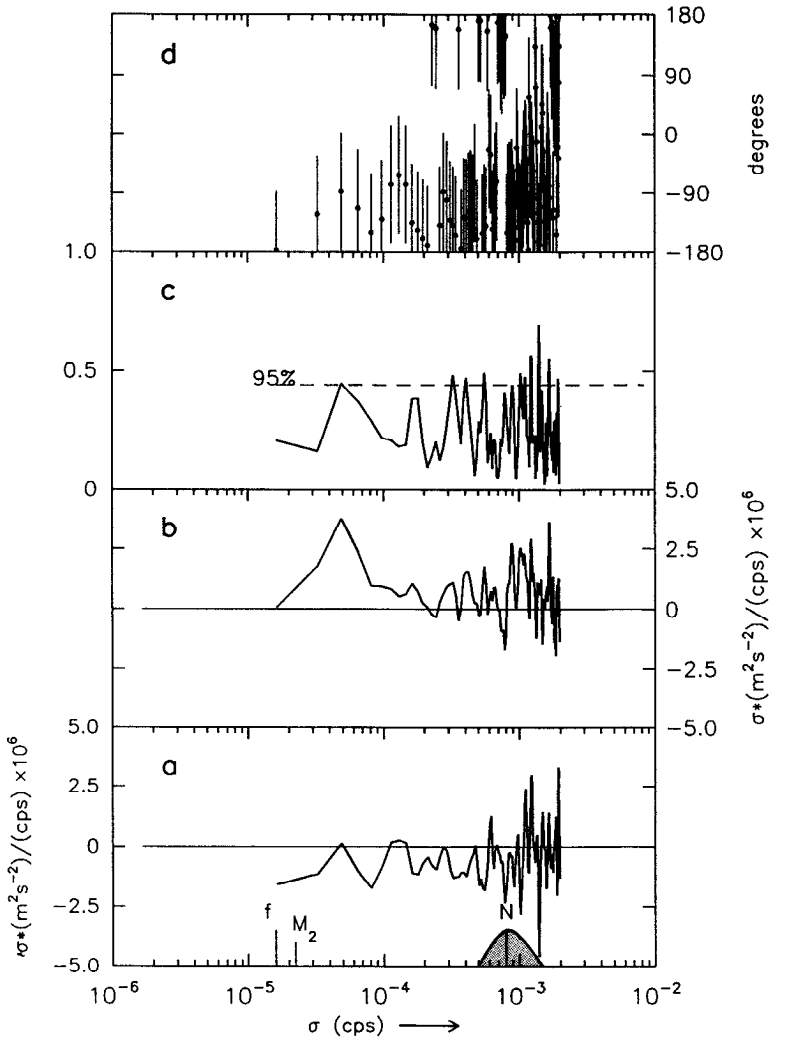

Figure 8. Example of cross-spectral information between $\hat{v}$ and the modified $\hat{w}$ as in (7) at bin 8 (z = 12 m) for the full length of the experiment. (a) Cospectrum. (b) Quadrature spectrum. (c) Coherence spectrum. (d) Phase spectrum. Smoothing as for Figure 7; confidence intervals are not shown in (a) and (b) as they may be inferred from (c) and (d). The significance level in (c) is computed according to $c = [1 - \beta^{1/(n-1)}]^{1/2}$, with $1 - \beta = 95\%$ the confidence level and n half the number of degrees of freedom (Thompson, 1979).

194 profiles remained after processing, using the spectral method, which included averaging over 3.4 m depth intervals from the bottom upwards.

The dissipation rate has been inferred from microshear measurements under the assumption of isotropic turbulence ($\epsilon = 7.5\nu\ \overline{(\partial u''/\partial z)^2} = 7.5\nu\ \overline{(\partial v''/\partial z)^2}$, with ν the kinematic viscosity and the double prime denoting fluctuating velocity at turbulent

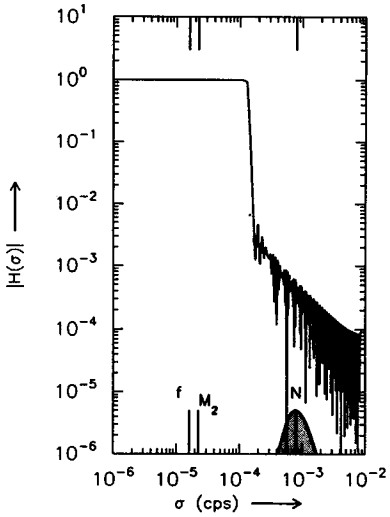

Figure 9. Amplitude response function for the symmetric low-pass filter used in flow separation (high-pass = 1 − low-pass).

dissipation scales). The guard near the sensors caused a relatively high noise level of $\epsilon_{noise} = 3 \times 10^{-9}$ W kg^{-1}.

The vertical eddy diffusivity for heat is defined under the assumption of isotropy as

$$K_T = \frac{1}{2} \frac{\chi_T}{(\partial \overline{T}/\partial z)^2},$$

with $\chi_T = 6D\overline{(\partial T''/\partial z)^2}$ a measure of temperature dissipation. D is the molecular diffusion constant. The noise level in $\chi_T \simeq 10^{-8}$ °C^2 s^{-1} and the accuracy to which $(\partial \overline{T}/\partial z)^2$ could be determined is about 10^{-7} (°C m^{-1})^2.

The ratio of the rates of change of potential and kinetic energies is a measure of the mixing efficiency

$$\Gamma = \frac{1}{2} \frac{N^2 \chi_T}{\epsilon (\partial \overline{T}/\partial z)^2}.$$

To avoid bias, mean values of Γ and K_T have been derived by computing them from the ratio of the mean numerator and denominator. Mean quantities for a certain part of the water column and a span of time have been calculated after noise reduction, which consisted of discarding all data at a sample point when one of the following criteria was met: $\epsilon \leq 2 \times 10^{-10}$ W kg^{-1}, $\chi_T \leq 5 \times 10^{-9}$ °C^2 s^{-1}, $N \leq 5 \times 10^{-4}$ s^{-1} ($\partial \overline{T}/\partial z \leq 2 \times 10^{-4}$ °C m^{-1}). Because of the high noise level in ϵ, these data were resampled when $\epsilon \leq 3 \times 10^{-9}$ W kg^{-1} using a random generator to obtain (any) value in the range $[3 \times 10^{-11}, 3 \times 10^{-9}]$ W kg^{-1}.

As none of the statistical distributions of ϵ, χ_T resembled log-normality, before or

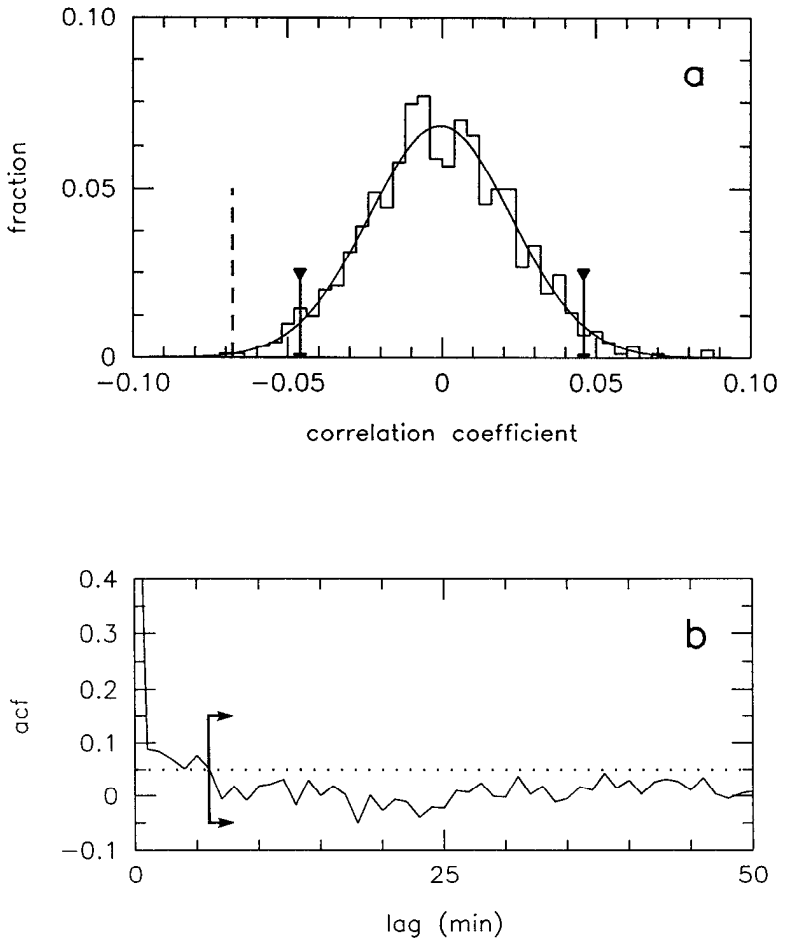

Figure 10. (a) Example of measured stress estimate (heavy dashed line) and the "error" distribution (histogram) obtained by computing the correlation coefficient 1000 times at random lag. The solid line is a Gaussian curve fitted on the distribution. The 95% significance levels are indicated by the posts. The estimate shown is for cross-isobath direction, N-band, $\alpha = 0.024$, $z = 12$ m. (b) The autocorrelation function (acf) of the stress estimate as a function of lag. The zone near lag 0 for which the acf > 0.05 is excluded from the error distribution in (a).

after noise correction, a bootstrap method was used to determine the confidence levels about the means. We will discuss actual values of these microstructure-derived quantities later in the context of the equation of turbulent kinetic energy.

5. Bottom boundary layer observations

Time series of the horizontal current show a prevailing along-isobath component and a dominant tidal signal (Fig. 11a). Isotherm displacements (Fig. 11b) have

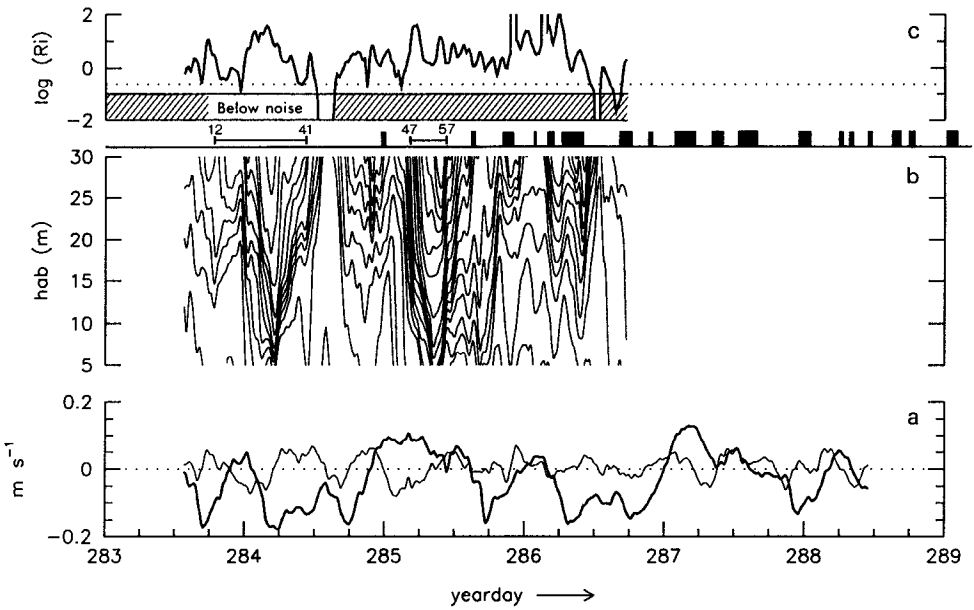

Figure 11. Hourly mean time series. (a) Horizontal current components $\hat{u}$ (thick) and $\hat{v}$ (thin) measured at $z = 12$ m. These records closely resemble those obtained after averaging over $8 < z < 17$ m. (b) Isotherms at 0.1°C intervals. (c) Gradient Richardson number Ri computed according to (13) between $z = 8$ and 18 m. $Ri = 10^{-2}$ when $\Delta T/\Delta z \geq 0°\text{C m}^{-1}$. The dotted line shows $Ri_{\text{crit}} = 0.25$. Periods of microstructure profiling are indicated by solid rectangles, together with two sequences when CTD profiles were obtained every half hour near the mooring (stations 12–41 and 47–57).

amplitudes greater than 30 m and the height of a well-mixed near bottom layer varies rapidly between less than 4 m and larger than 30 m, similar to observations made by Thorpe (1987) and Thorpe *et al.* (1990), although to a smaller vertical extent here. Isotherms are steeper when they rise during the upslope phase of the tide. The rate of rise is interrupted by short-term (1 h) periods of isotherm flattening, or restratification.

Temperature increases toward the bottom. The *T-S* relation is reasonably tight between 100–200 m depth, except for small short-term variations, and temperature and density relate according to $\Delta\rho = (0.127 \pm 0.006)\,\Delta T$ kg m^{-3}, computed from 69 CTD profiles. Thus a local bulk gradient Richardson number Ri can be calculated, from thermistor chain and ADCP data, as

$$Ri = \frac{-0.127 g \Delta T \Delta z}{\bar{\rho}[(\Delta\hat{u})^2 + (\Delta\hat{v})^2]} \tag{13}$$

where g is the acceleration of gravity and $\bar{\rho}$ denotes the average density. This serves as a measure for flow stability and can be compared with the canonical critical value of $Ri_{\text{crit}} = 0.25$, although this is not a prerequisite condition for advective instability

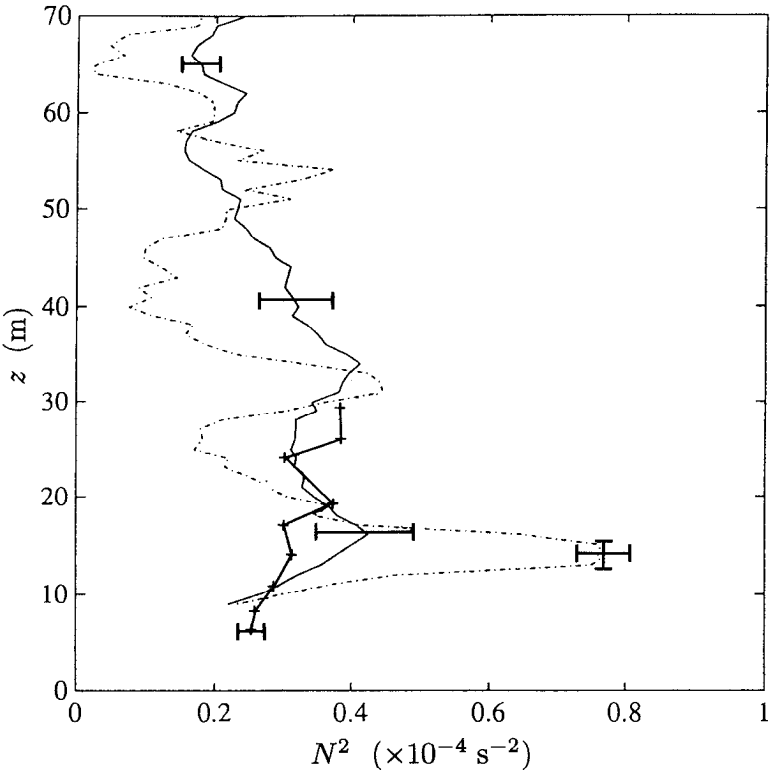

Figure 12. Squared buoyancy frequency profiles as obtained by finite differencing density data from CTD stations over 5-m intervals. The solid line indicates the profile averaged over stations 12–41 and 45–56. The dashed-dot line is the profile for station 31 (day 284.23), with the error bars computed from the instrument's accuracy. The + indicate N^2 values obtained from the thermistor string records, by using $\Delta\rho = 0.127\Delta T$.

when wave steepness is large (Thorpe, 1978). The *Ri* estimates shown in Figure 11c are somewhat crude because the resolution of the thermistor chain is 0.022°C and hence, for a typical shear value of 5×10^{-3} s^{-1}, $Ri \simeq 0.1$ is the minimum detectable over a 10 m range. In general *Ri* is larger than its critical value. A few periods of near critical stability occur, mostly when temperature gradients are weak and with frequent temperature inversions.

The average stratification rate decreases with height above the bottom towards a minimum at about $z = 60$ m (Fig. 12). Expected low N^2-values are not found near the bottom, which indicates that we did not resolve the well-mixed boundary layer with the CTD which was stopped at about 5 m above the bottom. Multiple marginally stable layers of vertical extent between 1–5 m are observed especially during periods when the isotherms are close to the bottom (Fig. 13). Persistently stable layers seem to organize near $z \simeq 15$ and 35 m, but the natural variability of the smaller scale

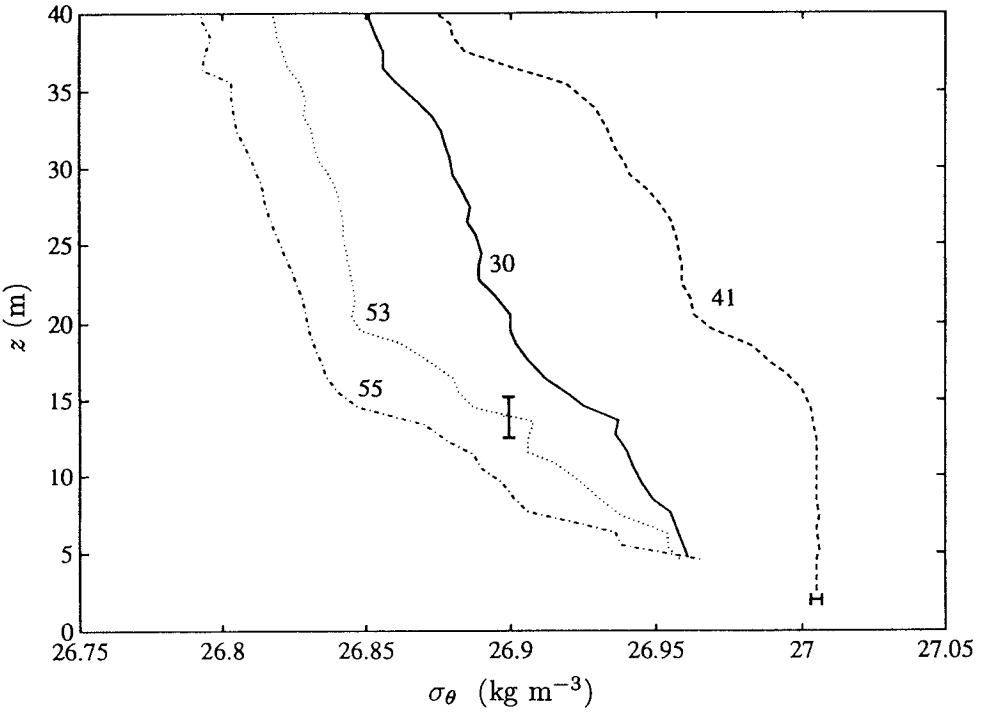

Figure 13. Density profiles from CTD stations 30 (day 284.22), 41 (284.44), 53 (285.29) and 55 (285.33).

layering and the inaccuracy of absolute CTD-depth determination prohibit an unbiased observation, as may be seen from comparison of a typical N^2-profile from a single station and an average profile from several stations (Fig. 12).

a. Bottom boundary heights. Estimates of the average mixed layer height δ and the mixing layer height h have been calculated from data obtained via the microstructure profiler that reached the bottom. Here δ is defined as the height at which the temperature first reaches a value that is lower than the bottom temperature plus a constant increment ΔT accounting for the instrument's accuracy. The δ estimated in this way will depend heavily on the choice of ΔT, as shown by Lentz and Trowbridge (1991). A reasonable, albeit ambiguous, choice seems to be twice the instrument's noise level which gives $\Delta T = 0.005$°C. The mixing layer height h is defined as the height where the dissipation is reduced to a value of $\bar{\epsilon}_t = 5 \times 10^{-9}$ W kg^{-1}, which is twice the background value. This choice is also rather arbitrary, but it is the best estimate of the level where the turbulent kinetic energy approaches zero, the more appropriate choice (Dewey *et al.*, 1988). It is noted that this definition may not provide a correct estimate of h when bottom frictional and breaking internal wave turbulent layers do not overlap.

After averaging over those profiles that have been obtained in water with depths between 170 and 190 m, we find

$$\delta = 3.0 \pm 0.3 \text{ m}$$
$$h = 9.6 \pm 0.9 \text{ m},$$

where the standard error (68% significance level) has been determined using a bootstrap method. The distributions of individual estimates were highly skewed. The ratio $h/\delta > 1$ indicates that bottom boundary layer mixing might be effective. (Although increasing ΔT to 0.050 °C and with $\bar{\epsilon}_t$ as above gives an expected mean ratio of about 1.8 m.) The values for δ and h also indicate that our moored data are mostly obtained above these layers, but the uncertainty is fairly large. They are considerably lower than those found by Dewey *et al.* (1988) in water similar in depth and current velocity, but above a flat bottom. They reported typical heights of 30 m and a ratio of 1.

In the situation that prevails here, with turbulent mixing apparently extending beyond the thickness of a bottom homogeneous layer, it is appropriate to estimate this thickness from Thorpe's (1987) formula, written in a different form here as

$$\delta \approx \Delta_f (1 + SPr)^{-1/4}, \tag{14}$$

where $\Delta_f = (2A/f)^{1/2}$ is the Ekman depth above a flat bottom, A is the eddy viscosity, N the 'interior' buoyancy frequency, Pr the eddy Prandtl number and S the Burger number. With the estimate $A \simeq 9 \times 10^{-3}$ m^2 s^{-1} (Section 6c) one finds $\Delta_f \simeq 13$ m. Reducing this by a factor of 4 to achieve $\delta = 3$ m requires, given $S \simeq 1.4$, Pr of $O(100)$, not inconsistent with the small estimates of eddy diffusivity that we will later obtain from the levels of turbulent microstructure.

The variability of the bottom boundary layer thickness in space and time is apparent in Figure 14, in which an example of a quasi-synoptic cross-isobath section of microstructure data is displayed. This figure also shows the short scale variability in isotherm displacement and relatively large dissipation rate values very close to the bottom as well as (extending) well above it. It took about 70 min to complete this transect while the ship drifted at an average speed of 0.3 m s^{-1}.

In summary, the data suggest a thin well-mixed layer embedded in a thicker mixing region which is subject to buoyancy-driven restratification on a slope. Steady state theory predicts for a downwelling favorable along-isobath mean flow (negative u) a positive upslope flow near the bottom and a downslope flow just above, as the "secondary circulation" within the mixing region, (Phillips *et al.*, 1986; Garrett, 1990). Additionally, a flow convergence or, "tertiary circulation," is expected within h where a pycnocline meets the bottom.

b. Mean currents. The five-day average of horizontal current is nearly constant with depth in the along-isobath direction with $\bar{\hat{u}} = -3.1 \pm 0.1$ cm s^{-1}, except for $\bar{\hat{u}} =$

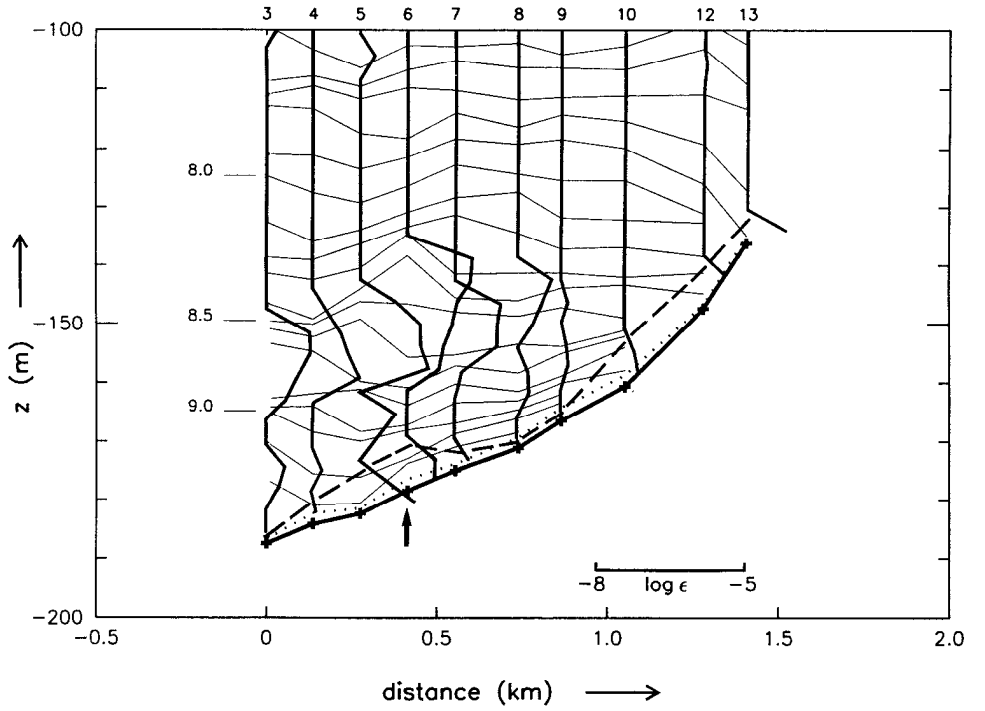

Figure 14. Quasi-synoptic cross-isobath section of temperature (thin contour lines every 0.1°C) and dissipation rate (thick profiles windowed between $10^{-8} < \epsilon < 10^{-5}$ W kg^{-1}). The mixed layer height δ (dotted line) and mixing layer height h (dashed line) are defined in the text. This example transect was recorded at day 286.2, while the ship drifted along a cross-isobath track about 1.5 km to the southwest of the mooring, the depth of which is indicated by the arrow.

-2.5 cm s^{-1} at the current meter. In the cross-isobath direction $\bar{v}$ increases linearly from 0.0 at $z = 8$ m to 1.1 cm s^{-1} at 21 m above the bottom and drops to 0.5 cm s^{-1} at the current meter ($z = 31$ m). This is somewhat difficult to match with the downwelling favorable along-isobath flow (the sign of $\bar{v}$ is "wrong"). Alternatively, a mean Eulerian flow can be generated as a response to a Stokes drift, but Ou and Maas (1986) predicted that this flow should also be directed downslope. Hypothetically an upslope $\bar{v}$ (with negative $\bar{u}$) could be found just below a region of strong mixing or where an interior pycnocline meets the slope, provided that the "tertiary" circulation induced by the variable properties is stronger than the local "secondary" circulation due to boundary mixing (Phillips *et al.*, 1986).

6. Flux estimates

a. Significant stresses. Figure 15 displays stress estimates $-(\overline{u'w'})_b$, $-(\overline{v'w'})_b$ from (7) and $-\overline{(\hat{u}'\hat{w}')}$, $-\overline{(\hat{v}'\hat{w}')}$, for different slope angles. With z perpendicular to the

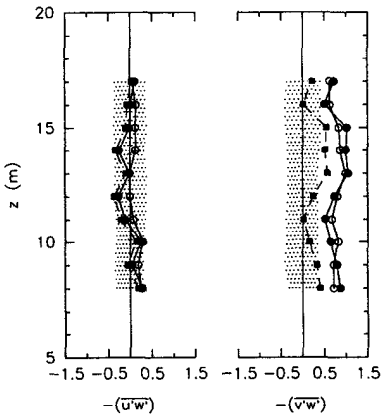

Figure 15. Reynolds stress estimates from (7) (in 10^{-5} m^2 s^{-2}) as a function of z for the fluctuating flow with $\sigma > 2 \times 10^{-4}$ cps (N-band), averaged over the period between days 284.3–287.7. Results for z perpendicular to the measured slope ($\alpha = 0.024$) are shown by —●—, those for $\alpha = 0.0$ by —■—. The horizontal extent of the dotted area represents the 95% significance levels from the error distributions (cf. Fig. 11). The 'direct' stress estimates $-\overline{(\hat{u}'\hat{w}')}$, $-\overline{(\hat{v}'\hat{w}')}$ for $\alpha = 0.024$ are given by —○—

slope at angle $\alpha = 0.024$, stress estimates significantly different from zero are found, but only in the cross-isobath direction. Cross-slope stress estimates are larger than along-isobath components. If bottom friction accounted for this stress one would expect the largest stress component in the along-isobath direction, but it is too weak to be significantly measured. Accepting a noise value of 3×10^{-6} m^2 s^{-2} and using a drag coefficient $C_D = 2.5 \times 10^{-3}$, one expects $U_{100} \simeq 3.5$ cm s^{-1}, which approximates the extrapolated (stress effective) current amplitude at $z = 1$ m. Although we have not resolved the bottom topography sufficiently, the observed stress magnitudes are not thought to be a result of topographic lee wave generation, which is estimated at 3×10^{-6} m^2 s^{-2} or less (Section 4b). The observed anisotropy in stress estimates indicates that part of the cross-slope eddy momentum flux is thus probably induced by internal wave reflection or some other instability-generating mechanism that does not affect the along-isobath flux.

Little difference exists between stress estimates made under the assumption of either statistical or current homogeneity over the beam spread: both show the same level of statistical significance and so the assumption of current homogeneity is fair, indicating that structures responsible for this flux have length scales exceeding the beam spread. We proceed with estimates under the statistical homogeneity assumption and neglect the insignificant along-isobath stress estimates.

The slope angle dependence of stress estimates is visualized by rotating the y, z-plane by $\varphi_2 = -0.024$ (the latter gives $-z$ in the direction of gravity, so that $\alpha = 0.0$). The impact of rotation over this tiny angle is stunning, albeit in accordance with (8) and confirming the notion that the contribution of the variance of

$\hat{v}'$ (approximating $\overline{\hat{v}'\hat{v}'}$ by $\overline{\hat{v}'^2}$), probably induced by N-band internal waves, is larger than the covariance between $\hat{u}'$ and $\hat{v}'$ since most dramatic changes occur in the cross-isobath direction. Vertically $\overline{\hat{v}'^2}$ changes little and the cross-isobath stress estimates vary approximately linearly with the rotation angle by $\Delta[-(\overline{v'w'})_b] \approx 1.8\Delta\varphi_2 \times 10^{-4}\,\mathrm{m^2\,s^{-2}}$.

For the important choice of the proper coordinate system, an independent test was performed. Although more appropriate, we could not determine α by varying the pitch angle $\overline{\varphi_2}$ (Fig. 4) to minimize the average buoyancy flux, because these flux estimates were barely statistically significant (see below). Also, we could not determine α by finding $\overline{\varphi_2}$ for zero $\overline{\hat{w}}$ as attempts to do so gave ambiguous results due to instrumental bias. One needs data closer to the bottom. However, we found that minimizing the variance of $\hat{w}$ gave $\overline{\varphi_2} = 0.018 \pm 0.004$. As this is not greatly different from the measured slope ($\alpha = 0.024$) it seems that the latter is sufficiently accurately determined and that the cross-isobath stress estimates are significantly different from zero and least contaminated by (internal) wave variance, when z is in the bottom normal direction.

b. Internal wave reflection. Measurement of the Reynolds stresses is important in its own right. However, to treat them as an indication of turbulence and relate them to the gradient of the mean flow, we should rule out the possibility that they are associated with freely propagating, non-breaking, internal waves.

A single internal wave would of course, have a Reynolds stress in any coordinate frame. This stress would be removed in the geodetic frame, however, either by horizontal isotropy of the wave field, or by vertical isotropy as for perfect reflection from a flat bottom. Rotating the vertical axis to be bottom-normal induces anisotropy in the internal wave field, but it is easy to show that, even without the effect of horizontal isotropy, the correlation between v and w becomes very small for waves near N due to (i) a reflection coefficient near 1 if the critical frequency for the bottom slope is very much less than N and (ii) a vertical wavelength that is larger than the distance to the bottom. (If it is not, then the horizontal wavelength near N would be comparable with the beam separation and show up in a bigger difference between $\hat{w}$ and $\hat{e}$ than observed.)

Further calculations for model spectra are desirable, but we provisionally conclude that the computed N-band correlations between v and w are not a manifestation of internal waves in that frequency band, but rather evidence for a Reynolds stress associated with turbulence, perhaps induced by the internal tide or by the bottom reflection of waves of lower frequency that are intensified on reflection.

c. Fluxes and mean gradients. A possible relation between stress and mean-flow shear has been tested from data according to $-(\overline{v'w'})_b = A(\overline{\partial\hat{v}})/(\partial z)$, where A denotes the eddy viscosity, by differencing the mean cross-isobath current components of the bins

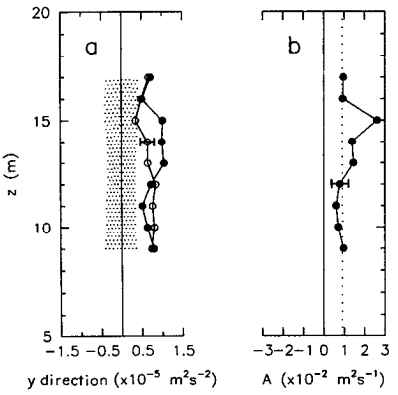

Figure 16. Comparison of cross-isobath stress estimates $-(\overline{v'w'})_b$ with the mean-flow shear as a function of z, averaged over a period between days 284.3–287.7 and for $\alpha = 0.024$. (a) Stress is indicated by —●— and $A \times$ (shear) by —○—. A constant eddy viscosity of $A = 9 \times 10^{-3}$ m^2 s^{-1} is used. The dotted area is as in Fig. 15. (b) Ratio of stress estimates and mean-flow shear. The thin dotted line indicates $A = 9 \times 10^{-3}$ m^2 s^{-1}.

immediately neighboring the bin of a stress estimate. A nearly constant value of $A = 9 \pm 3 \times 10^{-3}$ m^2 s^{-1} is inferred from values of the ratio of stress and mean-flow shear for depths outside the region near $z = 14$ m, where values are 1.5–2 times larger (Fig. 16). It seems that, even in a tidal regime, a correspondence between mean-flow shear and N-band stress exists. Confidence is gained by the fact that in general A is positive, implying momentum flux down the gradient.

Buoyancy flux estimates $-\overline{w'\rho'}$ have been calculated according to (12) for $\alpha = 0.024$ and averaged over the period between days 284.3–286.0. They are not significantly different from zero at the 95% level, except at $z = 15$ m (Fig. 17). The flux appears countergradient.

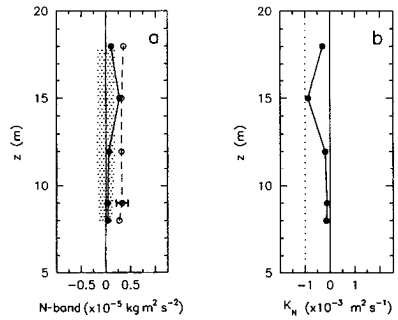

Figure 17. Buoyancy flux estimates $-\overline{w'\rho'}$ according to (12) compared with $K(\overline{\Delta\rho})/(\Delta z)$ for $\alpha = 0.024$. The density is calculated from the temperature records ($\Delta\rho = 0.127\Delta T$). The averaging period is from days 284.3–286.0. (a) $K \times$ (mean gradient) is indicated by —○—, $K = -10^{-3}$ m^2 s^{-1} and the buoyancy flux by —●—. The unit is 10^{-5} kg m^{-2} s^{-2}. (b) The ratio $-\overline{w'\rho'}/(\overline{\Delta\rho}/\Delta z)$ is shown by —●— and $K = -10^{-3}$ m^2 s^{-1} by ···· The unit is 10^{-3} m^2 s^{-1}.

An estimate of the eddy diffusivity would be $K = -10^{-3}$ m^2 s^{-1} at $z = 15$ m and less in magnitude at other depths. This gives an estimate of the eddy Prandtl number of $O(-10)$. On the other hand, an average eddy diffusivity, determined from microstructure data, is $\overline{K_T} = 2.2 \pm 0.7 \times 10^{-4}$ m^2 s^{-1}, approximately constant between $8 < z < 20$ m. With this estimate for K we find $Pr = O(100)$. Given the estimates for the mixed layer depth, this explains why we did not find significant buoyancy flux estimates at depths other than $z = 15$ m. The large K-value found from direct flux measurements at the latter depth is not reproduced in microstructure data, perhaps due to unfortunate sampling as we see in Section 6g. Only very close to the bottom (at $z = 2$ m) and above steeper slopes does the microstructure profiler give values of K_T up to 10^{-3} m^2 s^{-1}.

d. Flux divergence and circulation. The steady state equations (Phillips *et al.,* 1986), describing the mean flow and buoyancy above an infinite slope without along-slope variations, are

$$-f\bar{v} = -\frac{\partial}{\partial z}(\overline{u'w'})_b \tag{15}$$

$$f\bar{u} = -\frac{\partial}{\partial z}(\overline{v'w'})_b + \bar{B}\sin\alpha - \frac{1}{\rho_0}\frac{\partial \bar{p}}{\partial y} \tag{16}$$

$$0 = -\frac{\partial}{\partial z}(\overline{w'^2}) + \bar{B}\cos\alpha - \frac{1}{\rho_0}\frac{\partial \bar{p}}{\partial z} \tag{17}$$

$$\bar{\hat{w}}\frac{\partial \bar{B}}{\partial z} + \bar{\hat{v}}\frac{\partial \bar{B}}{\partial y} = \frac{g}{\rho_0}\frac{\partial}{\partial z}(\overline{w'\rho'}), \tag{18}$$

where $\bar{B}(z, t) = -g(\bar{\rho}(z,t) - \rho_0)/\rho_0$ with ρ_0 a reference density and $\bar{p}(z)$ is the mean pressure minus the pressure in a reference fluid of density ρ_0 at rest. We cannot test (15) with our data because the along-isobath stress estimates are below the level of statistical significance. Eliminating the unknown pressure gradient terms in (16) and (17) gives

$$f\frac{\partial \bar{u}}{\partial z} = \frac{\partial \bar{B}}{\partial z}\sin\alpha - \frac{\partial \bar{B}}{\partial y}\cos\alpha - \frac{\partial^2}{\partial z^2}(\overline{v'w'})_b, \tag{19}$$

where the cross-isobath gradient of the Reynolds stress component $\overline{\hat{w}'^2}$ is assumed to vanish, under the assumption of homogeneity in the (x, y) plane. In fact, one requires that all mean properties, except buoyancy, are independent of y above an infinite, constant slope. Hence, the first term in (18) should vanish also. This may not be valid for our data, as we shall see.

Firstly, we consider the familiar thermal wind balance, for which the last term on

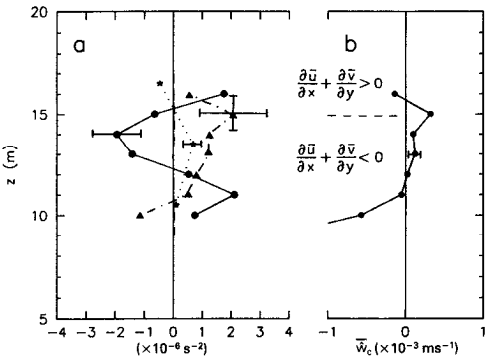

Figure 18. (a) Mean momentum shear balance (20), where $f\,\partial\bar{\hat{u}}/\partial z$ from (19) is included (– – –), for days 284.3–287.7. Term $-\partial^2(\overline{\hat{v}'w'})_b/\partial z^2$ (Δz = 2 m) is denoted by —●— with the standard error bar computed from the significance levels in Figure 14 under the assumption of a normal distribution (Fig. 10). The buoyancy gradient term $\partial\bar{B}/\partial z(\sin\alpha + \bar{\hat{w}}_c/\bar{\hat{v}}\cos\alpha)$ (- · ▲ - ·) is computed (with the appropriate correction on $\bar{\hat{w}}$, see Section 4a) from (ADCP data and) CTD profiles 12–41, 45–56 with Δz = 2 m. The buoyancy flux term $-g/(\rho_0\bar{\hat{v}})\,\partial(\overline{w'\rho'})/\partial z$ is given by · ∗ · (b) Profile of the corrected mean bottom-normal velocity component and inferred regions of horizontal flow divergence.

the right-hand side of (19) should be small with respect to the other two. The mean current shear is typically only 1 to 5 × 10^{-4} s^{-1}. If we take, following Phillips *et al.* (1986), $\partial\bar{B}/\partial y = N^2 \sin\alpha$, where N^2 is understood as the mean 'interior' buoyancy gradient, we require $\partial\bar{B}/\partial z - N^2\cos\alpha \leq 10^{-6}\ s^{-2}$ (nearly flat isopycnals) for this weak shear to be in thermal wind balance in (19). Given the measured buoyancy gradients of $O(10^{-5})\ s^{-2}$ (Fig. 13), it seems more likely that the buoyancy gradient term in (19) is $O(10^{-5})\ s^{-2}$ too, so that mixing must destroy the mean (along-isobath) current shear.

In order to verify this we use (18) to estimate $\partial\bar{B}/\partial y$. Investigation of the (corrected; cf. Section 4a) mean bottom-normal velocity $\bar{\hat{w}}_c(z)$ and the (coarse) estimate of the right-hand side of (18) indicate that the latter is $O(10^{-1})$ to $O(1)$ times the first term in (18). Hence, the bottom-normal velocity cannot be neglected and an advective buoyancy balance seems appropriate except near the pycnocline. Then (19) becomes

$$0 \simeq \frac{\partial\bar{B}}{\partial z}\left(\sin\alpha + \frac{\bar{\hat{w}}_c}{\bar{\hat{v}}}\cos\alpha\right) - \frac{g}{\rho_0\bar{\hat{v}}}\frac{\partial(\overline{w'\rho'})}{\partial z} - \frac{\partial^2}{\partial z^2}(\overline{\hat{v}'w'})_b. \qquad (20)$$

The uncertainty in the buoyancy gradient amounts to 60–100% as estimated after averaging CTD profiles, in large part due to the environmental variability over time and the imperfect depth determination with the CTD. Despite the large errors, the terms in (20) are of the same order of magnitude and roughly show the correct signs for a balance (Fig. 18). The bottom-normal velocity is positive in the zone between

12–16 m, roughly where the largest buoyancy gradient is found. Below 15 m, a convergence in horizontal velocity is anticipated from continuity. If we assume negligible along-slope divergence, this suggests a tertiary boundary layer circulation (Phillips *et al.,* 1986), as was also inferred from the mean currents in Section 5b. We recall that this may be a manifestation of the steep slope nearby, and the observed mean bottom-normal velocity values are fairly large.

e. What causes $\overline{w}$*?* Following Phillips *et al.* (1986) or Garrett (1991), the outflow to be expected in a region of varying interior stratification $N^2(z)$ can be expressed as a mean bottom-normal velocity

$$\overline{w} = -K_{\text{eff}} h \frac{d}{dz}\left(\frac{1}{N^2}\frac{dN^2}{dz}\right)$$

where K_{eff} is the effective vertical eddy diffusivity relating the vertical buoyancy flux in the mixing region of thickness h to the interior stratification N^2. It would give outflow from the boundary layer into the interior at the maximum of N^2.

In the present situation, with mixing extending well outside the well-mixed bottom boundary layer, we may take K_{eff} to be roughly as given by the turbulence data, i.e. $O(10^{-4})$ m^2 s^{-1} and h about 10 to 20 m. We do not have CTD data for $N^2(z)$ at relevant depths away from the bottom, but historical data suggest that N^2 varies rapidly with height and $N^{-2}\, dN^2/dz$ is about (30 m)$^{-1}$ and an order of magnitude larger in thin layers (Section 5). Hence we expect $\overline{w}$ to be $O(10^{-6}$ to $10^{-5})$ m^2 s^{-1}. The pattern of $\overline{w}$ that we observe shows larger values, suggesting that it arises from other causes, possibly due to along-slope flow divergence that is neglected in simple models.

f. Kinetic energy budget. The fluxes estimated from ADCP (and thermistor chain) data may be compared with microstructure data. We consider the approximate "turbulent" kinetic energy balance

$$\underset{\text{(a)}}{-(\overline{v'w'})_b \frac{\overline{\partial \hat{v}}}{\partial z}} \underset{\text{(b)}}{- \overline{(\langle v'w' \rangle)_b \frac{\partial(\langle \hat{v} \rangle - \bar{\hat{v}})}{\partial z}}} \underset{\text{(c)}}{- \frac{g}{\bar{\rho}} \overline{w'\rho'}} \underset{\text{(d)}}{= \bar{\epsilon}} \qquad (21)$$

where $\bar{\epsilon}$ is the average viscous dissipation rate, $\langle\ \rangle$ denotes averaging over the "turbulence" (N-band) time scale and the overbar denotes averaging over the total time span of measurements. Along-isobath terms are left out because these stresses are small. Also not included are terms describing a redistribution of turbulent energy, as is common in oceanic energy budgeting (e.g. Osborn, 1980). With respect to the usual model such as Osborn's, an extra term (b) is included to account for the shear production by waves. Somewhat along the lines for coherent structures in a

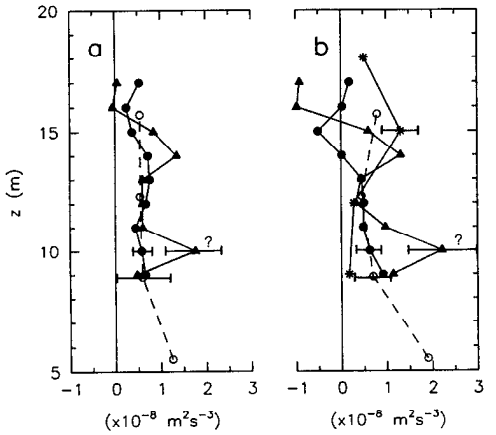

Figure 19. Estimates of terms in the turbulent kinetic energy equation (21), for N-band fluctuating quantities and $\alpha = 0.024$. Cross-isobath stress and mean-flow shear production (a) is shown by —●— and the cross-isobath stress and tidal wave shear production (b) by —▲—. Buoyancy production (term (c) divided by 2) is given by —*—. The average dissipation rate (term (d) divided by 2), indicated by —○—, is inferred from microstructure data obtained in water depths between 170 and 190 m ($\alpha \simeq 0.024$). (a) Averaging period between days 284.3–287.7 ($n = 60$ microstructure profiles). (b) Averaging period between days 284.3–286.0 ($n = 11$).

turbulent flow (Hussain, 1983), the flow is decomposed into three parts: the mean, the tides and internal waveband generated turbulence, where the latter is defined as flows with frequencies $\sigma > 2 \times 10^{-4}$ cps.

Given the data set, it is assumed that most of the turbulence is generated by internal waveband stress and dissipated at microstructure scales. The balance (21) may point at a (time averaged) local balance between shear stress production, buoyancy production and dissipation, but the neglect of redistributing terms prevents a precise space-time allocation of processes.

Thus, noting other assumptions underlying (21) as well, such as isotropy at dissipative scales, a balance not better than within a factor of 2 is anticipated (Oakey, 1982). Due to the shortness of the data records, errors in (b) will be fairly large. All dissipation rates considered here were measured above an approximately constant slope (α as before) near the mooring, i.e. in water with depths between 170 and 190 m, and averaged in time per 3.4 m height interval. Calculations have been made for two averaging periods, days 284.3–287.7 for a maximal data overlap but probably a poor estimate of the buoyancy term and days 284.3–286.0 during which hardly any dissipation data were obtained (Fig. 11).

The results on the estimates of (21) are ambiguous although the cross-isobath terms sufficiently explain the dissipation. The mean-flow shear turbulent production term (a) is approximately constant in the vertical and compares well with $\bar{\epsilon}/2$ (Fig. 19, Table 2). Estimates of tidal (M_2 *and* O_1) wave shear production (term (b)) are equal

Table 2. Estimates of terms ($\times 10^{-8}$ W kg^{-1}) in approximate turbulent kinetic energy balance (21), and average mixing efficiency $\bar{\Gamma}$ from microstructure data as a function of distance off the bottom (n = number of microstructure data in averaging period). The errors given represent the 68% confidence levels outside the mean values.

z(m)	(a) ± 0.1	(b) ± 0.3	(a + b) ± 0.4	(c) ± 0.8	$\bar{\epsilon}$	$\overline{\chi_T}$	$\bar{\Gamma}$	$\overline{K_T}$
Period: days 284.3–287.7						$n = 30$		
9	0.6	0.7	1.3	0.2*†	1.5 ± 0.3	2.0 ± 0.5	0.3 ± 0.1	1.3 ± 0.4
13	0.7	0.8	1.5	0.3*†	1.6 ± 0.2	2.2 ± 0.5	0.4 ± 0.1	2.1 ± 0.7
16	0.5	0.3	0.8	1.3*	1.4 ± 0.3	1.8 ± 0.5	0.5 ± 0.2	3.2 ± 1.0
Period: days 284.3–286.0						$n = 11$**		
9	0.7	1.2	1.9	0.4†	1.3 ± 0.2	0.9 ± 0.2	0.13 ± 0.04	0.4 ± 0.1
13	0.5	0.6	1.1	0.6†	1.6 ± 0.4	2.4 ± 0.7	0.4 ± 0.2	2.0 ± 0.8
16	−0.1	0.0	−0.1	2.6	2.0 ± 0.5	2.4 ± 0.9	0.4 ± 0.2	3.1 ± 1.5

*: Estimates available only for half this period; values assumed zero for second half.

**: Unreliable estimates as datapoints were available between days 285.5–286.0 only (cf. Fig. 12).

†: Buoyancy flux estimates not exceeding 95% level of significance.

in size and of the same sign as (a), but they are less accurately determined as they vary considerably in the vertical (Fig. 19). The sum of terms (a) and (b) compares well with $\bar{\epsilon}$, except near $z = 15$ m during the shorter period between days 284.3–286.0, when the buoyancy production (c) is large.

This region of enhanced restratification ($z \simeq 15$ m) seems to coincide with decreased work of stress against mean-flow shear and a relatively large loss of turbulent kinetic energy when the tidal current shear is large (Fig. 19b). In general a balance is found (within a factor of 2) between internal wave band production (with stress working against mean-flow shear) and viscous dissipation despite barely overlapping buoyancy and dissipation measurement periods. Dissipation rate data, averaged over the same 3.5-day period, measured very close to bottom, and interior values found above bottoms with depths less than 165 m (above the steep slope $\alpha = 0.12$), give values higher by an order of magnitude than the ones shown in Figure 19 and Table 2.

The eddy diffusivity values are calculated from microstructure data and an order of magnitude smaller than found by Thorpe (1987). Average mixing efficiency values $\bar{\Gamma}$ are about twice the canonical value $\Gamma = 0.25$ (Oakey, 1982) outside the near-bottom and interior regions (not shown), but the errors are large (Table 2).

g. A time series of flux estimates. Our data records are too short to investigate the time evolution of flux estimates and to determine the effect of the internal wave band on tides. It is possible, however, to obtain an impression of the time variability of fluxes when N-band estimates are obtained from averages over the shortest period possible (2 h). Figure 20 shows time series of such buoyancy and cross-isobath momentum

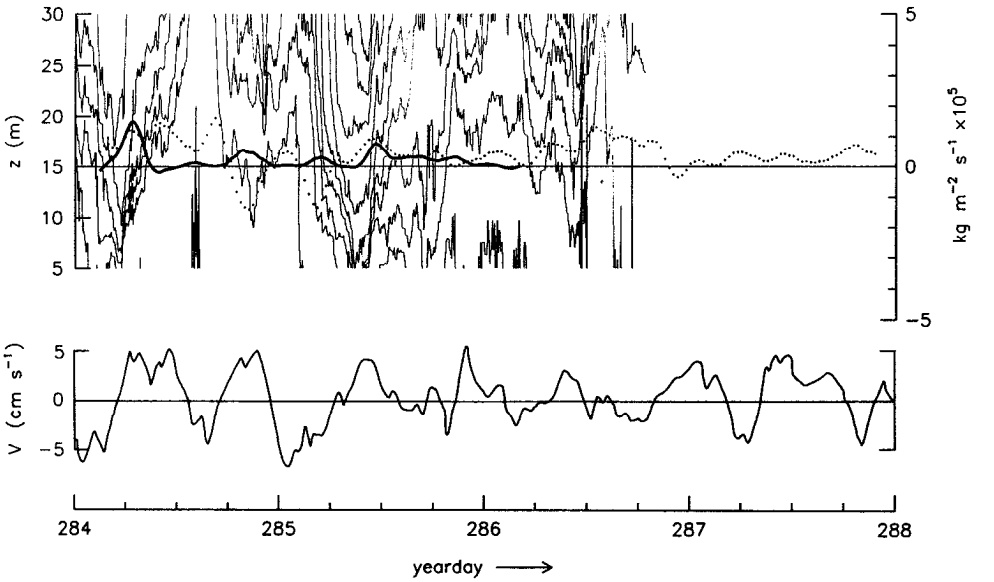

Figure 20. Isotherms (0.2°C, thin lines) from unfiltered temperature data are shown together with two-hourly smoothed time series of $-\langle w'\rho' \rangle$ (heavy solid lines, scale on the right) and $-(\langle v'w' \rangle)_b$ (dotted line, scale: $[-1, 1] \times 10^{-4}$ m^2 s^{-2}). Averaging, denoted by $\langle\ \rangle$, is over the N-band time scale. The flux estimates are for $z = 15$ m, N-band, $\alpha = 0.024$. On the lower axis one-hourly smoothed $\hat{v}$ has been redrawn from Figure 11.

fluxes for $z = 15$ m, $\alpha = 0.024$. This height represents the top of the average boundary layer. Error bars are left out and the following results are qualitative only.

The buoyancy flux shows peaks during relatively short periods of time when isotherms are steeply rising (days 284.3 and 285.45). Its tendency is to flatten the isotherms, sometimes in association with the occurrence of high frequency internal waves and during periods of $Ri \simeq 1$ (Fig. 20; compare with the smoothed isotherm plot in Fig. 11). Such periods occur twice, separated by 2.5–3 hours, during the rise of isotherms, the second time outside the range of ADCP data. Temperature records for the 5-day period obtained by sensors at the current meter and ADCP indicate that such strong events do not occur after day 286.7. Our pilot experiment does not provide an explanation for this variability in flux and (background) internal wave activity, but indicates the necessity of simultaneous sampling of data on microstructure and lower frequency motions in space and time. Here the kinetic energy budget (21) has not been resolved well.

Eddy momentum fluxes seem to be organized over longer periods of time with less pronounced peaks compared to the buoyancy fluxes, with an indication of larger positive values during periods of, or just after, the rise of isotherms. Their amplitudes also decrease somewhat after day 286.7.

The cause of the sharp rise of isotherms remains to be investigated. Perhaps it is

part of the reflection process of internal tides. Clearly the mixed layer development is quite different in a tidal regime (see also Thorpe, 1987) compared to regimes where lower frequency (periods of O(days)) motions are dominant (as derived by Weatherly and Martin, 1978; Lentz and Trowbridge, 1991). The latter authors show a strong relationship between the (sign of the) along-isobath current and the mixed layer height, with the largest values found during a downwelling-favorable flow. Such a relationship is not clear here. Figures 20 and 11 suggest some relation between tides and near N-band eddy fluxes through the upslope flow phase, but longer data records are required for quantification by ensemble averaging over the tidal period.

7. Conclusions

We have attempted to gain some observational insight in the specific mixing region above a sloping bottom from an experiment of relatively short duration. We conclude that

- above a sloping bottom eddy momentum fluxes are large enough to be detected significantly with a pulse-incoherent 1.2 MHz ADCP. The fluxes originate mainly near N, the local buoyancy frequency, with a local maximum near the pycnocline capping the bottom boundary layer ($z \simeq 15$ m). They are found in the cross-isobath direction only, possibly because the mean along-slope current is more or less independent of height so that mixing it does not produce significant fluctuations or stress. The stress values found are not a manifestation of bottom friction or topographic internal lee wave generation and are most likely associated with internal wave instability.

- if related to the mean flow shear, the momentum flux may be parameterized with an eddy viscosity $A \simeq 9 \times 10^{-3}$ m^2 s^{-1} within the boundary layer and about twice this value in the pycnocline. By considering the momentum (shear) equations, it appears that mixing prevents thermal wind shear from developing. In the buoyancy equation the bottom-normal advective term cannot be neglected, but the measured bottom-normal velocity is bigger than expected for the tertiary circulation in two-dimensional theories, and may be related to along-slope convergence. On the other hand, consideration of the mean flow profiles seems to point at the possibility as well of a tertiary circulation dominating over a secondary circulation.

- in an approximate turbulent kinetic energy budget, stress/mean shear and stress/tidal shear production are of equal size and roughly balance the turbulent dissipation rate within the boundary layer. At the height of the local pycnocline, buoyancy production is the main source.

- significant buoyancy fluxes are only found at the height of the local pycnocline and are countergradient. The contribution to the overall mean value comes

from short periods during which isotherms rise sharply (the upslope phase of the tide) and intense small-scale waves are found. Generally, the momentum flux is also large during such periods, although less pronounced. The relatively large average eddy diffusivity values, anticipated in bottom boundary layer theory, are not found.

Many questions on the efficiency of mixing above a sloping bottom remain unanswered. Perhaps some experimental evidence can be gained in another experiment, for which we recommend:

- Longer sampling to reduce statistical problems. A period of a month should be adequate.
- A steeper slope so that the results will depend less on the accurate measurement of the slope angle. In the along-isobath direction smooth, slowly varying bottom topography is preferred. This requirement may be harder to meet the steeper the slopes become.
- More accurate instruments such as a pulse-coded or pulse-to-pulse coherent Doppler sonar and more accurate thermistors, sampling at a faster rate ($O(10\ \text{s})$) to reach within the turbulence part of the spectrum. The latter, in combination with prolonged series in time, demands large but achievable data storage capacity of $O(100\ \text{MB})$.

In addition, larger spatial coverage would enable sampling of information on the directionality of waves and eddy fluxes and on the difference between Reynolds stresses in the frictional boundary layer and those found higher in the water column. The importance of a more accurate determination of (average) local buoyancy gradients is noted.

Acknowledgments. We thank the crew of C. S. S. *Dawson* for their cooperation during the field experiment. At BIO/Dartmouth, N.S., we thank Helen Hayden for her patience during the introduction of computer systems. We gratefully acknowledge the efforts of Don Belliveau to improve our understanding of troublesome ADCP data. Major turning points during the data analysis were given by Hidekatsu Yamazaki (SEOS/University of Victoria, B.C.) and Marc Fleury (Mulhouse, France) on statistics, and by Denis Gilbert (Mont Joli, Quebec) on the slope angle dependence of flux estimates. Rolf Lueck (SEOS) pointed out the correction for a spinning ADCP. Michael Ott provided programming assistance. We acknowledge Eric Kunze's (University of Washington) efforts in thoroughly criticizing an earlier draft of this paper and we thank anonymous referees for constructive reviews. Rosalie Rutka prepared the manuscript and some figures under hectic conditions.

This work was partially supported by grants from Canada's Natural Sciences and Engineering Research Council and the U.S. Office of Naval Research.

APPENDIX

Computing vertical Reynolds stress components from data measured by a slowly rotating ADCP

An ADCP, rotating about its vertical axis, indicated by a heading angle $\phi = \varphi_1(t)$ (Fig. 4), measures (per ping) beam velocity components $\hat{b}_i$ for any bin according to

$$\begin{aligned}
\hat{b}_1 &= -(u_1 \cos\phi - v_1 \sin\phi)\sin\theta - w_1 \cos\theta \\
\hat{b}_2 &= (u_2 \cos\phi - v_2 \sin\phi)\sin\theta - w_2 \cos\theta \\
\hat{b}_3 &= -(v_3 \cos\phi + u_3 \sin\phi)\sin\theta - w_3 \cos\theta \\
\hat{b}_4 &= (v_4 \cos\phi + u_4 \sin\phi)\sin\theta - w_4 \cos\theta,
\end{aligned} \tag{A.1}$$

which is an extended version of (2) where instrumental errors $\hat{\gamma}_i$ have been left out. In (A.1) each set $(u, v, w)_i$ of "true" velocity components denotes Cartesian velocity components at the location of a specific beam i. Hence, they are not measured, as a function of time, at fixed locations in the (x, y) planes, but at locations along the circle encompassing the centers of the four bins at a given depth. Beam average velocity components are computed from

$$\begin{aligned}
\hat{u} &= [(\hat{b}_2 - \hat{b}_1)\cos\phi + (\hat{b}_4 - \hat{b}_3)\sin\phi]/2\sin\theta \\
\hat{v} &= [(\hat{b}_4 - \hat{b}_3)\cos\phi - (\hat{b}_2 - \hat{b}_1)\sin\phi]/2\sin\theta \\
\hat{w} &= -\sum_{i=1}^{4} \hat{b}_i/4\cos\theta \\
\hat{e} &= (\hat{b}_1 + \hat{b}_2 - \hat{b}_3 - \hat{b}_4)/4\cos\theta,
\end{aligned} \tag{A.2}$$

or

$$\begin{aligned}
\hat{u} &= \tfrac{1}{2}[(u_1 + u_2)\cos^2\phi + (u_3 + u_4)\sin^2\phi + (v_3 + v_4 - v_1 - v_2)\sin\phi\cos\phi] \\
&\quad - [(w_4 - w_3)\sin\phi + (w_2 - w_1)\cos\phi]/2\tan\theta \\
\hat{v} &= \tfrac{1}{2}[(v_3 + v_4)\cos^2\phi + (v_1 + v_2)\sin^2\phi + (u_3 + u_4 - u_1 - u_2)\sin\phi\cos\phi] \\
&\quad - [(w_4 - w_3)\cos\phi - (w_2 - w_1)\sin\phi]/2\tan\theta \\
\hat{w} &= \sum_{i=1}^{4} w_i/4 - [(u_2 - u_1)\cos\phi + (u_4 - u_3)\sin\phi \\
&\quad + (v_4 - v_3)\cos\phi - (v_2 - v_1)\sin\phi]\tan\theta/4 \\
\hat{e} &= (w_3 + w_4 - w_1 - w_2)/4 - [(u_2 - u_1)\cos\phi - (u_4 - u_3)\sin\phi \\
&\quad - (v_4 - v_3)\cos\phi - (v_2 - v_1)\sin\phi]\tan\theta/4.
\end{aligned} \tag{A.3}$$

The Reynolds decomposition is somewhat problematic. The right-hand sides in (A.3) contain double and triple products of (probably) fluctuating quantities. The

low-pass filtered ('mean') flow is considered homogeneous over the beam spread so that

$$\bar{u} = \bar{u}_1 = \bar{u}_2 = \bar{u}_3 = \bar{u}_4, \qquad \text{similar for } \bar{v}, \bar{w},$$
$$\overline{u_i^+} = \overline{v_i^+} = \overline{w_i^+} = 0 \qquad i = 1, \ldots, 4,$$

and

$$\bar{\hat{u}} = \bar{u} + \tfrac{1}{2}[\overline{(u_3^+ + u_4^+ - u_1^+ - u_2^+)\sin^2\phi} + \overline{[(v_3^+ + v_4^+ - v_1^+ - v_2^+)\sin\phi\cos\phi]} - [\overline{(w_4^+ - w_3^+)\sin\phi} + \overline{(w_2^+ - w_1^+)\cos\phi}]/2\tan\theta, \tag{A.4}$$

where the plusses denote local deviations from the overall means $\bar{u}$, $\bar{v}$ and $\bar{w}$ as opposed to fluctuations resulting after high-pass filtering a time series measured at a fixed location. Equations similar to (A.4) are found for $\bar{\hat{v}}$, $\bar{\hat{w}}$ and $\bar{\hat{e}}$, with the notion that $\bar{e} = 0$ by definition. No direct method is available to test the importance of the terms in (A.4) containing local deviations. Here we assume that, on average, functions containing ϕ do not correlate with any of the parts of the fluctuating velocity components that are inhomogeneous over the beam spread, so that $\bar{\hat{u}} = \bar{u}$ (and similar for $\bar{\hat{v}}$, $\bar{\hat{w}}$, $\bar{\hat{e}} = 0$). Then we may use Eqs. (A.3), where all velocity components and no angles carry primes, as the appropriate equations for the fluctuating velocity components. This should enable us to obtain stress estimates for which statistics are homogeneous over the beam spread.

In order to compute these in terms of measured quantities, the primed ($\approx$ "fluctuating") beam velocity components may be reconstructed from the fluctuating velocity components,

$$\begin{aligned}
\tilde{b}'_1 &= -(\hat{u}'\cos\phi - \hat{v}'\sin\phi)\sin\theta - (\hat{w}' - \hat{e}')\cos\theta \\
\tilde{b}'_2 &= (\hat{u}'\cos\phi - \hat{v}'\sin\phi)\sin\theta - (\hat{w}' - \hat{e}')\cos\theta \\
\tilde{b}'_3 &= -(\hat{v}'\cos\phi + \hat{u}'\sin\phi)\sin\theta - (\hat{w}' + \hat{e}')\cos\theta \\
\tilde{b}'_4 &= -(\hat{v}'\cos\phi + \hat{u}'\sin\phi)\sin\theta - (\hat{w}' + \hat{e}')\cos\theta .
\end{aligned} \tag{A.5}$$

These beam velocities are indicated by a tilde here because they are not directly "measured" by the instrument and $\hat{b}_1 \neq \bar{\hat{b}}_1 + \tilde{b}'_1, \ldots$, in general.

The vertical Reynolds stress components, as defined for a non-rotating system in (4) and (6), are obtained by treating the cross-products as vector components with $(\tilde{b}_2'^2 - \tilde{b}_1'^2)$ in the direction of u and similarly for the v-component. The final results are in Eqs. (7) reproduced below

$$\begin{aligned}
-(\overline{u'w'})_b &= [\overline{(\tilde{b}_2'^2 - \tilde{b}_1'^2)\cos\phi} + \overline{(\tilde{b}_4'^2 - \tilde{b}_3'^2)\sin\phi}]/2\sin 2\theta \\
&= -\overline{\hat{u}'[\hat{w}' - \hat{e}'(\cos 2\phi - \hat{v}'/\hat{u}'\sin 2\phi)]} \\
-(\overline{v'w'})_b &= [\overline{(\tilde{b}_4'^2 - \tilde{b}_3'^2)\cos\phi} - \overline{(\tilde{b}_2'^2 - \tilde{b}_1'^2)\sin\phi}]/2\sin 2\theta \\
&= -\overline{\hat{v}'[\hat{w}' + \hat{e}'(\cos 2\phi + \hat{u}'/\hat{v}'\sin 2\phi)]}
\end{aligned} \tag{7}$$

Unfortunately, in practice (7) contains difficult terms in the triple products of velocities mainly due to finite bit resolution. These terms, involving the ratios of $\hat{v}'$ and $\hat{u}'$, cause the statistical uncertainty to blow up when the velocities approach zero. We dealt with this problem by (arbitrarily) restricting $[\hat{w}' - \hat{e}'(\cos 2\phi - \hat{v}'/\hat{u}' \sin 2\phi)]$, $[\hat{w}' + \hat{e}' (\cos 2\phi + \hat{u}'/\hat{v}' \sin 2\phi)] < 6(\overline{\hat{w}'^2})^{0.5}$, so that per bin about 4% of the data were rejected.

REFERENCES

Chereskin, T. K., E. Firing and J. A. Gast. 1989. Identifying and screening filter skew and noise bias in acoustic Doppler current profiler measurements. J. Atmos. Ocean. Tech., *6,* 1040–1054.

Dewey, R. K., P. H. LeBlond and W. R. Crawford. 1988. The turbulent bottom boundary layer and its influence on local dynamics over the continental shelf. Dyn. Atmos. Oceans, *12,* 143–172.

Eriksen, C. C. 1982. Observations on internal wave reflection off sloping bottoms. J. Geophys. Res., *87,* 525–538.

—— 1985. Implications of ocean bottom reflection for internal wave spectra and mixing. J. Phys. Oceanogr., *15,* 1145–1156.

Flagg, C. N. and S. L. Smith. 1989. On the use of the acoustic Doppler current profiler to measure zooplankton abundance. Deep-Sea Res., *36,* 455–474.

Garrett, C. 1990. The role of secondary circulation in boundary mixing. J. Geophys. Res., *95,* 3183–3189.

—— 1991. Marginal mixing theories. Atmos.-Ocean, *29,* 313–339.

Gilbert, D. and C. Garrett. 1989. Implications for ocean mixing of internal wave scattering off irregular topography. J. Geophys. Res., *19,* 1716–1729.

Gross, T. F., A. J. Williams III and W. D. Grant. 1986. Long-term *in situ* calculations of kinetic energy and Reynolds stress in a deep sea boundary layer. J. Geophys. Res., *91,* 8461–8469.

Heathershaw, A. D. and J. H. Simpson. 1978. The sampling variability of the Reynolds stress and its relation to boundary shear stress and drag coefficient measurements. Estuar. Coast. Mar. Sci., *6,* 263–274.

Hussain, A. K. M. F. 1983. Coherent structures—reality and myth. Phys. Fluids, *26,* 2816–2850.

Jenkins, G. M. and D. G. Watts. 1968. Spectral Analysis and its Applications. Holden-Day, San Francisco, 525 pp.

Lentz, S. J. and J. H. Trowbridge. 1991. The bottom boundary layer over the Northern California Shelf. J. Phys. Oceanogr., *21,* 1186–1201.

Lohrmann, A., B. Hackett and L. P. Røed. 1990. High resolution measurements of turbulence, velocity and stress using a pulse-to-pulse coherent sonar. J. Atmos. Ocean. Tech., *7,* 19–37.

MacCready, P. and P. B. Rhines. 1993. Slippery bottom boundary layers on a slope. J. Phys. Oceanogr., *23,* 5–22.

Munk, W. 1981. Internal waves and small-scale processes, *in* Evolution of Physical Oceanography, B. A. Warren and C. Wunsch, eds., MIT Press, Cambridge, Mass., 264–291.

Oakey, N. S. 1982. Determination of the rate of dissipation of turbulent energy from simultaneous temperature and velocity shear measurements. J. Phys. Oceanogr., *12,* 256–271.

—— 1987. EPSONDE: A deep ocean microstructure profiler. Proc. Oceans '87, 316–321.

Osborn, T. R. 1980. Estimates of the local rate of vertical diffusion from dissipation measurements. J. Phys. Oceanogr., *10,* 83–89.

Ou, H. W. and L. Maas. 1986. Tidal-induced buoyancy flux and mean transverse circulation. Cont. Shelf Res., *5,* 611–628.

Parks, T. W. and C. S. Burrus. 1987. Digital Filter Design. John Wiley & Sons, New York, 342 pp.

Phillips, O. M., J.-H. Shyu and H. Salmun. 1986. An experiment on boundary mixing: mean circulation and transport rates. J. Fluid Mech., *173,* 473–499.

Plueddemann, A. J. 1987. Observations of the upper ocean using a multi-beam Doppler sonar. PhD thesis, SIO Ref. 87-15, Scripps Institution of Oceanography, 103 pp.

RD Instruments. 1989. Velocity measurement bias errors in the ADCP. RDI-Tech. Bull. ADCP-89-06, 24 pp.

Schott, F. 1988. Effects of a thermistor string mounted between the acoustic beams of an acoustic Doppler current profiler. J. Atmos. Ocean. Tech., *5,* 154–159.

Schott, F. and W. Johns. 1987. Half-year-long measurements with a buoy-mounted acoustic Doppler current profiler in the Somali current. J. Geophys. Res., *92,* 5169–5176.

Thompson, R. O. R. Y. 1979. Coherence significance levels. J. Atmos. Sci., *36,* 2020–2021.

Thorpe, S. A. 1978. On the shape and breaking of finite amplitude internal gravity waves in a shear flow. J. Fluid Mech., *85,* 7–31.

—— 1987. Current and temperature variability on the continental slope. Phil. Trans. Roy. Soc. Lond., *A323,* 471–517.

—— 1992. The generation of internal waves by flow over the rough topography of a continental slope. Proc. Roy. Soc. Lond., *A439,* 115–130.

Thorpe, S. A., P. Hall and M. White. 1990. The variability of mixing on a continental slope. Philos. Trans. Roy. Soc. Lond., *A331,* 183–194.

Weatherly, G. L. and P. J. Martin. 1978. On the structure and dynamics of the oceanic bottom boundary layer. J. Phys. Oceanogr., *8,* 557–570.

Received: *20 May, 1992;* revised: *1 March, 1994.*